Centro Politécnico Superior, Universidad de Zaragoza

Trabajo Fin de Máster
Máster en Mecánica Aplicada
Posgrado en Ingeniería Mecánica y de Materiales

Desarrollo de un modelo de daño basado en la microesfera para tejidos biológicos fibrados

---

Autor: ***D. Pablo Sáez Viñas***

Director: ***Dr. Miguel Ángel Martínez Barca***
Área de Mecánica de Medios Continuos y Teoría de Estructuras.
Departamento de Ingeniería Mecánica.

Curso 2009/10
Zaragoza, Septiembre de 2010

DESARROLLO DE UN MODELO DE DAÑO BASADO EN LA MICROESFERA PARA TEJIDOS BIOLÓGICOS FIBRADOS

RESUMEN

Este trabajo fin de máster presenta un modelo de daño micro estructural para tejido vascular usando técnicas multiescala. El trabajo se centra en el comportamiento anisótropo de los tejidos biológicos fibrados y en especial en procesos de ablandamiento o daño.

Los tejidos biológicos tienen una composición compleja y muy variable. Algunos de ellos, los denominados tejidos biológicos blandos (vasos sanguíneos, globo ocular, etc.), suelen contener altas concentraciones de colágeno. Esta sustancia se presenta normalmente en forma de fibras, responsables de soportar en gran medida las cargas mecánicas que se producen sobre el tejido. Cuando éstos se deforman lejos de su estado fisiológico se produce el daño del mismo.

Con el objeto de estudiar este proceso se ha utilizado una aproximación micro estructural, o más concretamente un modelo basado en la microesfera, para incluir el comportamiento de las fibras. Se ha utilizado un modelo hiperelástico, definiendo una función energía de deformación (FED) en su forma desacoplada. La distribución de las fibras se ha incorporado a través de dos funciones de probabilidad, para tener en cuenta la distribución de las fibrillas alrededor de la orientación preferencial de las mismas. El comportamiento mecánico de cada una de las micro-fibras se ha modelado con dos FEDs diferentes. Además, se ha incorporado un modelo de daño a esta técnica de homogeneización, a través de una formulación termodinámica consistente, que se acopla directamente al modelo hiperelástico de las micro-fibras, para obtener el daño o ablandamiento del tejido. Gracias al modelo micro mecánico, cuando las fibras del material son deformadas, el ablandamiento del material sucede de una manera gradual gracias al daño progresivo de las fibrillas que componen las fibras de colágeno. El puente entre la escala micro y macro, se establece a través de una técnica de homogeneización computacional con una integración numérica a lo largo de la superficie de la esfera de radio unidad.

Dicho modelo se ha implementado en un código de elementos finitos a través de una subrutina de usuario de Abaqus. Se han ajustado los parámetros del modelo con ensayos experimentales y se han simulado diferentes casos y geometrías para comprobar el comportamiento del modelo. Por último, se ha simulado un proceso de angioplastia en una geometría real, donde los parámetros del modelo han sido ajustados con ensayos experimentales.

Contents

1 Introduction **5**

2 Basic theory framework **7**
2.1 Essential kinematics 7
2.2 Hyperelastic framework 8

3 Material model **11**
3.1 Micro-sphere based model 11
3.2 Inclusion of anisotropy 13
3.2.1 The von Mises distribution 13
3.2.2 The Bingham distribution 13
3.3 Material behavior 14
3.3.1 Mechanical behavior of the micro-fibers 15
3.4 Fitting material parameters and comparison 16
3.5 Damage model 23

4 Validation examples **27**
4.1 A displacement driven brick example 27
4.2 Thin perforated plate 29

5 Clinical application example: Simulation of angioplasty **33**

6 Conclusions **37**

A Obtention of stress and elasticity tensors **41**

Bibliography **45**

1 Introduction

Most biological soft tissues, and particularly blood vessels, are composed of networks of collagen fibrils bundles (Rhodin, 1980) embedded in an isotropic ground substance with a high water content, which provide a well known almost incompressible behavior (Carew et al., 1968; Chuong & Fung, 1984). More in dept, blood vessels have three main layers (see, e.g., (Fung, 1990)), intima, media and adventitia. Media is mainly composed of smooth muscle and sheets of collagen fibers oriented preferentially along the circumferential direction. The adventitia, composed basically by a more random distribution of collagen fibrils bundles and the intima is made up of a thin layer of endothelial cells. The preferred orientation of the collagen fibers are main responsible of the anisotropic response and a highly non-linear behavior as detailed in numerous works (see, e.g., (Fung, 1990), (Humphrey, 1995)). It is worth noting the random distribution within the differentiable orientation of the collagen fibers in each layer as mentioned above. This structure on the micro-level has an important relevance in order to characterize these materials as will be discussed later.

Many constitutive models have been proposed over the last years to characterize biological tissues, to model them in incompressible or quasi-incompressible hyperelastic frameworks. In this context, the description of a given material comes from the definition of a strain energy function (SEF) from which all the mechanical relations and variables can be obtained. Early SEFs in soft tissue mechanics were purely phenomenological, whereby non micro-structural information is gathered, so they just were able to describe some aspects of the material and, usually, only under physiological loads. However, many of them have been widely used to this purpose with really satisfactory results (Demiray et al., 1988). In order to provide a more realistic characterization of the tissue, structural models, in which a structural tensor is introduced in the free energy function to take into account the anisotropy of the material (see, e.g., (Boehler, 1987; Holzapfel et al., 2005; Menzel & Steinmann, 2003)), were proposed to deal with these limitations. Although it was an advance on the mechanical characterization of materials, and soft tissue in particular, many of the latest works about these topics are going toward a more micro structural characterization and therefore micro-structural

models. Probably due to the improvements on the experimental field which have led to get information to feed these models. For example, the works of Ateshian (2007) and Taber (1998) are related to growth of the micro constituents, Kuhl & Holzapfel (2007) and Himpel et al. (2008) presented some results on the remodeling of collagen and elastin. Moreover, Gasser et al. (2006) and later Menzel et al. (2007) included micro-structure information into the hyperelastic formulation through the assumption of a statistical distribution of the fiber orientation around a preferential direction. In short, the high complexity of biological tissues requires mechanical models that include information of the underlying constituents and look for the physics of the whole processes within the material. The behavior of the micro-constituents can be taken into the macroscopic models by means of computational homogenization. It is in this context where the micro-sphere-based approach takes on a higher relevance. Miehe et al. (2004) used the micro-sphere approach with emphasis on elastomer and Alastrué et al. (2009a) carried it out applied to biological tissue.

Usually, the use of these models to characterize this kind of tissues are limited to the range of physiological loads or elastic regions. Most of the finite element implementations carried out up today have been limited to these regions and just few of them deal with the failure of soft tissues. Damage over biological tissues is an important issue when dealing with these materials. Some physiological processes, as aneurysm or over-stretching of tendons, or clinical surgeries as angioplasties or clamping could lead to damage of the material. Damage in soft biological tissue could be produced by the progressive failure or softening of either the matrix or the fibers. In this way some authors have proposed damage models for only one component of the material (fibers or matrix), applied to transversal anisotropy of soft tissue (Natali et al., 2005; Ehret & Itskov, 2009; Peña & Doblaré, 2009).

In this work, a three-dimensional decoupled finite strain formulation with a multi-scale model for the anisotropic part incorporating continuum damage is presented. The damage model is introduced both in the matrix and the collagen fibers. Though the damage along the fibers have been showed the most main issue, the damage over the matrix can not be avoided for a real modeling of the material. With the micro-structural incorporation a more realistic response of the damage evolution is hoped due to a transition of the damage in the micro scale from fibril to fibril all over the micro-sphere surface.

The work is organized as follows. In Chapter 2 the basis of the mechanical framework is presented. Chapter 3 deal with the material model, including the micro-sphere approach, the mechanical behavior, the anisotropy and the damage models. Chapter 4 present some numerical examples with some sensitivity analysis of parameters in different geometries. Chapter 5 shows the results of a clinical interest example, and finally, Chapter 6 present the conclusions of this work.

2 Basic theory framework

2.1 Essential kinematics

Let Ω_0 be the reference or material configuration of a continuum body $\mathcal{B}$ and Ω the current or spatial configuration at time t, regarding an arbitrary reference system (Cartesian since now on). Let $\mathbf{X} \in \Omega_0$ be the position of a particle in the reference configuration and $\mathbf{x} \in \Omega$ the position of the same particle at time t. The non-linear application $\varphi : \mathbf{X} \to \mathbf{x}$ that relates the position of $\mathbf{x}$ to $\mathbf{X}$, $\mathbf{x} = \varphi(\mathbf{X})$ is called motion map. The gradient of φ respect to $\mathbf{X}$, $\mathbf{F} = \nabla_{\mathbf{X}}\varphi$, represents the deformation gradient bi-point tensor. The Jacobian of the motion, J, is given by $J = \det(\mathbf{F})$.

In order to reproduce the quasi-incompressible behavior of soft tissues, an uncoupled representation of the SEF is used (Flory, 1961). The multiplicative decomposition of the deformation gradient and the Cauchy-Green tensor $\mathbf{C} = \mathbf{F}^T \cdot \mathbf{F}$ can be expressed as

$$\mathbf{F} = [J^{1/3}\mathbf{I}] \cdot \overline{\mathbf{F}} \tag{2.1}$$

$$\mathbf{C} = [J^{2/3}\mathbf{I}] \cdot \overline{\mathbf{C}} \tag{2.2}$$

where the terms $J^{1/3}\mathbf{I}$ and $J^{2/3}\mathbf{I}$, with $\mathbf{I}$ the second order unit tensor, are associated with changes of volume while $\overline{\mathbf{F}}$ and $\overline{\mathbf{C}}$, the isochoric deformation gradient and Cauchy-Green tensors, respectively, representing the volume-preserving part.

Furthermore, let $\mathbf{r} \in \Omega_0$ be a vector of the reference configuration. The motion map turns this vector, with the so called push-forward operation, into $overline\mathbf{t} \in \Omega$. Assuming $\mathbf{r}$ is affected just by the isochoric part of $\mathbf{F}$

$$\bar{\mathbf{t}} = \overline{\mathbf{F}} \cdot \mathbf{r} = J^{-1/3}\mathbf{t} \text{ with } \|\bar{\mathbf{t}}\| = \overline{\lambda} = J^{-1/3}\|\mathbf{t}\| \tag{2.3}$$

$\bar{\mathbf{t}}$ corresponds to the isochoric push-forward of the material vector $\mathbf{r}$ and $\bar{\lambda}$ to the isochoric stretch in the direction of $\mathbf{r}$.

2.2 Hyperelastic framework

As far as the free energy function is concerned, given an scalar-valued function Ψ defined per unit reference volume in the reference configuration and for isothermal processes, (Flory, 1961; Spencer, 1954) postulate the additive decoupled representation of the SEF in a volumetric and an isochoric part as

$$\Psi = \Psi_{\text{vol}} + \Psi_{\text{ich}} \tag{2.4}$$

As was discussed in the introduction, soft biological tissue is a highly non-linear anisotropic material. To differentiate between the isotropic and the anisotropic parts, the free energy function can be split up again as follow

$$\Psi = \Psi_{\text{vol}} + \Psi_{\text{iso}} + \Psi_{\text{ani}} \tag{2.5}$$

where Ψ_{vol} describes the free energy associated to changes of volume, Ψ_{iso} is the isotropic contribution of the free energy usually associated to the extracellular matrix, and Ψ_{ani} takes into account the anisotropy of the material.

Stress and elastic tensors can be obtained from the strain energy function just deriving it with respect to $\mathbf{F}$ once and twice respectively (see Truesdell & Noll (2004) and Menzel & Steinmann (2003) for a complete review of anisotropic hyper-elasticity).

Taking the free energy in function of $\mathbf{F}$, $\Psi(\mathbf{F})$ as the starting point, and under the premise that $\Psi(\mathbf{F})$ is an objective function and independent of rotation motion, it is possible to write $\Psi(\mathbf{F}) = \Psi(\mathbf{C})$ which lead to the second equality of the following equation defined as

$$\mathbf{P} = \frac{\partial \Psi(\mathbf{F})}{\partial \mathbf{F}} = 2\mathbf{F} \cdot \frac{\partial \Psi(\mathbf{C})}{\partial \mathbf{C}} = \mathbf{F} \cdot \mathbf{S} \tag{2.6}$$

and

$$\boldsymbol{\sigma} = \boldsymbol{\sigma}_{\text{vol}} + \boldsymbol{\sigma}_{\text{ich}} = 2J^{-1}\mathbf{F} \cdot \left[\frac{\partial \Psi_{\text{vol}}(J)}{\partial \mathbf{C}} + \frac{\partial \Psi_{\text{ich}}(\boldsymbol{C})}{\partial \mathbf{C}} \right] \cdot \mathbf{F}^T, \tag{2.7}$$

$$\boldsymbol{\tau} = J\boldsymbol{\sigma} = 2\mathbf{F} \cdot [\mathbf{S}_{\text{vol}} + \mathbf{S}_{\text{ich}}] \cdot \mathbf{F}^T, \tag{2.8}$$

where $\mathbf{P}$ is the first Piola-Krichhoff stress tensor, $\mathbf{S}$ is the second Piola-Krichhoff stress tensor with $\mathbf{S}_{\text{vol}}$ and $\mathbf{S}_{\text{ich}}$ the volumetric and isochoric part respectively, $\boldsymbol{\sigma}$ is the Cauchy stress tensor and $\boldsymbol{\tau}$ the Kirchoff stress tensor. These equation are often presented in terms of invariants I_1, I_2 and I_3 (first, second and third invariant respectively) for the isotropic part and I_4 and I_6 for the anisotropic part, see i.e Holzapfel (2000) and Spencer (1954) to a complete review of equations.

And in a similar way and assuming the elasticity tensor in the spatial configuration, defined as the push-forward of $boldsymbol\mathsf{C}$ multiply by J^{-1}

$$\mathsf{C} = \mathsf{C}_{\text{vol}} + \mathsf{C}_{\text{ich}} = 2 \left[\frac{\partial \mathbf{S}_{\text{iso}}(\mathbf{C})}{\partial \mathbf{C}} + \frac{\partial \mathbf{S}_{\text{ich}}(\mathbf{C})}{\partial \mathbf{C}} \right] \tag{2.9}$$

$$\mathbf{c} = J^{-1}\chi_*(\mathbf{C}) \tag{2.10}$$

with $\mathbf{c}_{\text{vol}}$ and $\mathbf{C}_{\text{ich}}$ the volumetric and isochoric part of the material elasticity tensor.

3 Material model

3.1 Micro-sphere based model

During the last years the most widely way of modeling anisotropy in soft tissue have been the use of vectors as fiber through an invariant formulation. Lately, the use of a orientation distribution functions has increased and it is the solution adopted in the present work. Furthermore, a micro-sphere-based approach has been incorporated in order to evaluate different variables in a micro-scale level.

The micro-sphere approach consist of getting the micro-structural information and move it into the macroscopic behavior carrying out a homogenization scheme on the unit sphere $\mathbb{U}^2$. This homogenization lies in a discretization of m directions $\{\mathbf{r}^i\}_{i=1...m}$ over the surface of the sphere, weighted by factors $\{w^i\}_{i=1...m}$, where $\langle\mathbf{r}\rangle \approx \sum_{i=1}^{m} w^i\mathbf{r}^i = 0$ and $\langle\mathbf{r}\otimes\mathbf{r}\rangle \approx \sum_{i=1}^{m} w^i\mathbf{r}^i\otimes\mathbf{r}^i = \frac{1}{3}\mathbf{I}$. So a integral over the unit sphere $\mathbb{U}^2$ can be discretized as follow

$$\langle(\bullet)\rangle = \frac{1}{4\pi}\int_{\mathbb{U}^2}(\bullet)\mathrm{dA} \approx \sum_{i=1}^{m} w^i(\bullet)^i \tag{3.1}$$

The 4π term, used to normalize, turns up as result of the surface integral $\int_0^\theta\int_0^\phi \sin(\theta)\,\mathrm{d}\theta\mathrm{d}\phi$ over the unit sphere $\mathbb{U}^2$. The unit vectors can be expressed in terms of the spherical angles $\theta\in[0,\pi)$ and $\phi\in[0,2\pi)$ as $\mathbf{r} = \sin(\theta)\cos(\phi)\mathbf{e}_x + \sin(\theta)\sin(\phi)\mathbf{e}_y + \cos(\phi)\mathbf{e}_z$ where $\{\mathbf{e}_x,\mathbf{e}_y,\mathbf{e}_z\}$ is the reference Cartesian system. Previous authors (Bažant & Oh, 1986; Alastrué et al., 2009a) have checked out different number of integration directions and in view of the results therein, a 368 direction will be used in all the problems simulated in this work since it demonstrated a good approximation (see results in Alastrué et al. (2009a)). The stereographic projection (3.1) is a useful tools in order to the values on the integral directions.

As detailed above, the anisotropic part of the SEF is related to the fibers in the material. In a general situation with N families of fibers the anisotropic part of the SEF can be expressed as

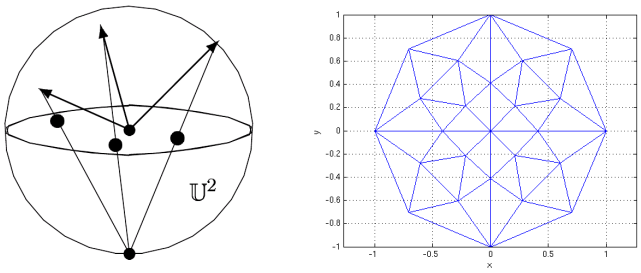

(a) Procedure to get stereographic projection. (b) Stereographic projection 21 directions.

$$\Psi_{\text{ani}} = \sum_{j=1}^{N} \Psi_f^{\text{j}} = \sum_{j=1}^{N} \left[\frac{1}{4\pi} \int_{\mathbb{U}^2} n\rho_{\text{f}}\psi_{\text{f}} dA \right] \tag{3.2}$$

where Ψ_{f}^{j} is the strain energy function for the j-nth family, ρ_{f} a statistical value associated with the fibrils dispersion, that will be discussed later, and ψ_{f} the free energy function of the fiber. In view of these considerations it is natural to adopt an affine assumption as far as the integration directions concern (compare Miehe et al. (2004)), in spite of what model is used for the micro fibers, as for example a non-affine eight-chain model (Arruda & Boyce, 1993). Since an analytical integration of (3.3) is not determined in a general case, a discretization of this equation is used

$$\Psi_{\text{ani}} \approx \sum_{j=1}^{N} \left[\sum_{i=1}^{m} n\rho_i w^i \psi(\overline{\lambda}_i) \right] \tag{3.3}$$

where $\overline{\lambda}_i$ and $\psi(\overline{\lambda}_i)$ is the stretch ratio and the free energy function associated to each integration direction

In order to obtain the macroscopic contribution to the Kirchhoff stresses and the elasticity tensor for a family of fibers, the SEF has been presented in terms of principal stretches, rather than the classical invariant's function (Ogden, 1996). The equations for the Kirchhoff stress tensor and the elasticity tensor in the spatial configuration are

$$\boldsymbol{\tau}_f = \sum_{i=1}^{m} [n\rho_i \psi_i'(\overline{\lambda}_i)^{-1} \bar{\mathbf{t}} \otimes \bar{\mathbf{t}}] w^i \tag{3.4}$$

$$\mathbf{c}_f = \sum_{i=1}^{m} [n\rho_i [\psi_i'' - \psi_i'(\overline{\lambda}_i)^{-1}](\overline{\lambda}_i)^{-2} \bar{\mathbf{t}} \otimes \bar{\mathbf{t}} \otimes \bar{\mathbf{t}} \otimes \bar{\mathbf{t}}] w^i \tag{3.5}$$

A detailed obtaining process is given in Appendix A.

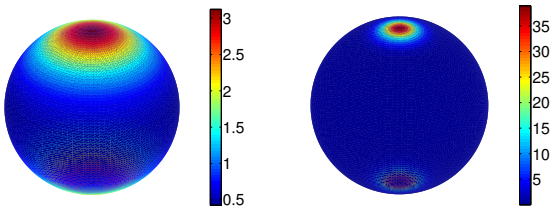

(c) b=1. (d) b=10.

Figure 3.1: Shape of the von Mises ODF for b=1 and b=10.

3.2 Inclusion of anisotropy

3.2.1 The von Mises distribution

This orientation distribution function is denoted by ρ and has some interesting properties such symmetry condition $\rho(\mathbf{r};\mathbf{a}) = \rho(-\mathbf{r};\mathbf{a})$ and rotation symmetry with respect to the preferred orientation $\mathbf{a}$, which can be expressed as $\rho(\mathbf{Q}\cdot\mathbf{r};\mathbf{a}) = \rho(\mathbf{r};\mathbf{a})\ \forall\mathbf{Q} \in \mathbb{Q}^3_+$. Note that $\mathbf{a}$ could be oriented in any direction of the space leading to a mismatch angle $w = \arccos(\mathbf{r}.\mathbf{a})$ different from those defined by θ and ϕ. A π-periodic von Mises ODF (3.6) has been adopted in this work to take into account the fibrils dispersion (Alastrué et al., 2009a).

$$\rho(\theta) = 4\sqrt{\frac{b}{2\pi}}\frac{\exp(b(cos(2\theta)+1))}{\text{erfi}(\sqrt{2b})} \tag{3.6}$$

where the concentration parameter $b \in \mathbb{R}^+$set a measure of the anisotropy with $b \to 0$ representing an isotropic material and $b \to \infty$ and ideally 1D fiber and erfi(x) is the imaginary error function approximated by a sufficiently large number of terms within its MacLaurin series expansion, which can be written as

$$erfi(x) \approx \pi^{-1/2}\left[2x + \frac{2x^3}{3} + \sum_{j=3}^{k}\frac{x^{2j-1}}{a(j)}\right] \tag{3.7}$$

with $a(j) = 0.5[2j-1][j-1]!$ (compare Weisstein (2004)) which provide with a 60 term expansion sufficient accuracy for values of $b \leq 20$. Fig. 3.1 show some distributions for different values of b as example of what kind of shapes present the concentration parameter.

3.2.2 The Bingham distribution

The Bingham (1974) ODF was used to account for the dispersion of the collagen fibrils with respect to their preferential orientation. That function is expressed as

$$\rho(\mathbf{r};\,\mathbf{A})\,\frac{\mathrm{d}A}{4\,\pi} = [K(\mathbf{A})]^{-1}\,\exp\left(\mathbf{r}^{\mathrm{t}}\cdot\mathbf{A}\cdot\mathbf{r}\right)\frac{\mathrm{d}A}{4\,\pi}, \tag{3.8}$$

where $\mathbf{A}$ is a symmetric $3x3$ matrix, $\mathrm{d}A$ is the Lebesgue invariant measure on the unit sphere, $\mathbf{r} \in \mathbb{U}^2$ and $K(\mathbf{A})$ is a normalizing constant. As its main features, it is worth noting that this distribution always exhibits antipodal symmetry, but not rotational symmetry for the general case (Bingham, 1974).

Applying straightforward transformations, Eq. (3.8) can be rewritten as

$$\rho(\mathbf{r};\, \mathbf{Z},\, \mathbf{Q})\, \frac{\mathrm{d}A}{4\,\pi} = \left[F_{000}(\mathbf{Z})\right]^{-1} \mathrm{etr}\left(\mathbf{A} \cdot \mathbf{A}^{\mathrm{t}} \cdot \mathbf{r} \cdot \mathbf{r}^{\mathrm{t}} \cdot \mathbf{Q}\right) \frac{\mathrm{d}A}{4\,\pi}, \tag{3.9}$$

where $\mathrm{etr}\,(\bullet) \equiv \exp\left(\mathrm{tr}\,(\bullet)\right)$, $\mathbf{Z}$ is a diagonal matrix with eigenvalues $\kappa_{1,2,3}$, $\mathbf{Q} \in \mathbb{Q}^3$ such that $\mathbf{A} = \mathbf{Q} \cdot \mathbf{Z} \cdot \mathbf{Q}^{\mathrm{T}}$ and $F_{000}(\mathbf{Z})$ may be written as

$$F_{000}(\mathbf{Z}) = \left[4\,\pi\right]^{-1} \int_{\mathbb{U}^2} \mathrm{etr}\left(\mathbf{Z} \cdot \mathbf{r} \cdot \mathbf{r}^{\mathrm{t}}\right) \mathrm{d}A = {}_1F_1(\frac{1}{2};\, \frac{3}{2};\, \mathbf{Z}), \tag{3.10}$$

with ${}_1F_1$ a confluent hyper-geometric function of matrix argument as defined by Herz (1955).

Thus, the probability concentration is controlled by the eigenvalues of $\mathbf{Z}$, which might be interpreted as concentration parameters. Specifically, the difference between pairs of $\kappa_{1,2,3}$ – i.e., $[\kappa_1 - \kappa_2]$, $[\kappa_1 - \kappa_3]$ and $[\kappa_2 - \kappa_3]$ – determines the shape of the distribution over the surface of the unit sphere. Therefore, the value of one of these three parameters may be fixed to a constant value without reducing the versatility of (3.9). Figure 3.2 shows different distributions of the fiber bundles concentration achieved for a constant value of κ_1 and varying values of κ_2 and κ_3. With this assumption, the distribution can expand along the plane composed of the associated direction with κ_2 and κ_3. As seen in Fig. 3.2(a) and (b), setting two of the parameters equal to zero the Von Mises ODF is obtained. The highest value of the parameters lead to the preferential orientations as shows Fig. 3.2(c) and (f). As two parameters come close up to a value a rotational symmetry is achieved.

3.3 Material behavior

As discussed above, the definition of a given material in the hyperelasctic modeling framework lies in the setting of free energy functions associated to each part of the above discussed splitting.

$$\Psi = \Psi_{\mathrm{vol}}(J) + \Psi_{\mathrm{iso}}(\overline{I}_1) + \Psi_{\mathrm{ani}}(n, \rho, \bar{\lambda}) \tag{3.11}$$

$$\Psi_{vol}(J) = \frac{1}{D}\ln^2(\mathrm{J}) \tag{3.12}$$

$$\Psi_{iso}(\overline{I}_1) = \mu[\overline{I}_1 - 3] \tag{3.13}$$

$$\Psi(n, \rho, \bar{\lambda}) = \langle n \rho_f \psi_f \rangle \tag{3.14}$$

The ground substance is known to be composed by a high water content, which results in an almost incompressible behavior, so the volumetric part of the energy function supposed force the quasi-incompressibility depending on the value

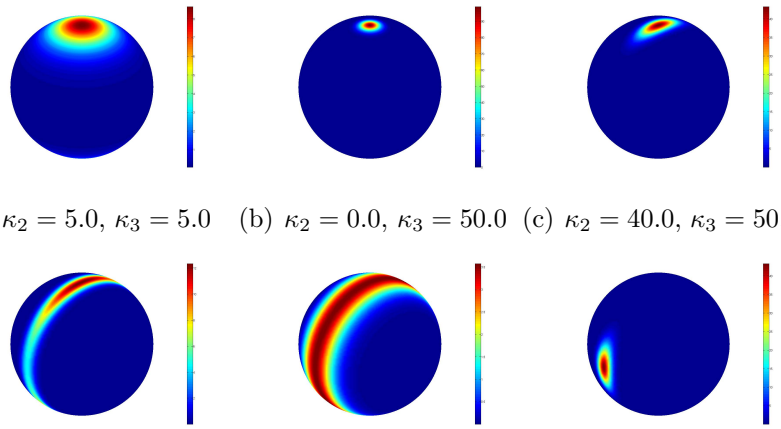

(a) $\kappa_2 = 5.0$, $\kappa_3 = 5.0$ (b) $\kappa_2 = 0.0$, $\kappa_3 = 50.0$ (c) $\kappa_2 = 40.0$, $\kappa_3 = 50.0$

(d) $\kappa_2 = 49.0$, $\kappa_3 = 50.0$ (e) $\kappa_2 = 10.0$, $\kappa_3 = 10.0$ (f) $\kappa_2 = 50.0$, $\kappa_3 = 49.0$

Figure 3.2: Representation of the Bingham ODF for different sets of parameters with $\kappa_1 = 0.0$.

of the penalty parameter D (3.12). The matrix contributes to the overall behavior through the volumetric and the isotropic part of the energy function (3.13).

Regarding the anisotropic part of the model (3.14), two statistical dispersion functions of the fibers, around a preferential orientation, are considered .

3.3.1 Mechanical behavior of the micro-fibers

Two microscopic strain energy density functions were used to model the contribution of the collagen fibrils to the macroscopic mechanical quantities (Alastrué et al., 2009a). First, a phenomenological exponential function frequently used to model the fiber response from a macroscopic phenomenological approach (Holzapfel et al., 2000), namely

$$n\Psi_{\mathrm{f}}^{i}(\bar{\lambda}_i) = \begin{cases} 0 & \text{if} \quad \bar{\lambda}_i < 1 \\ \dfrac{k_1}{2k_2}\left[\exp\left(k_2\left[\bar{\lambda}_i^2 - 1\right]^2\right) - 1\right] & \text{if} \quad \bar{\lambda}_i \geq 1 \end{cases} \tag{3.15}$$

where k_1 is a stress-valued constant, k_2 is a dimensionless parameter, and $\overline{\lambda}_i$ denotes the isochoric stretch in the fiber direction of $\mathbf{r}^i$, i.e., $\overline{\lambda}_i = \|\overline{\mathbf{t}}^i\|$.

The particularization of the eight-chain model (Arruda & Boyce, 1993) to the transversely isotropic case (Kuhl et al., 2006; Alastrué et al., 2009a) was also used

to model microfiber contributions, i.e.:

$$n\Psi_{\mathrm{f}}^{i}(\bar{\lambda}_i) = \begin{cases} 0 & \text{if} \quad \bar{\lambda}_i < 1 \\ \dfrac{n\,K\Theta\,L}{4\,A}\left[2\,\dfrac{\bar{r}_i^2}{L^2} + \dfrac{1}{1-\bar{r}_i/L} - \dfrac{\bar{r}_i}{L}\right. & \\ \left. -\dfrac{\ln(\bar{\lambda}_i^{4\,r_0^2})}{4\,r_0\,L}\left[4\,\dfrac{r_0}{L} + \dfrac{1}{[1-r_0/L]^2} - 1\right] - \Psi_{\mathrm{r}}\right] & \text{if} \quad \bar{\lambda}_i \geq 1 \end{cases} \tag{3.16}$$

with $\bar{r}_i = \bar{\lambda}_i\, r_0$, and

$$\Psi_{\mathrm{r}} = 2\,\frac{r_0^2}{L^2} + \frac{1}{1-r_0/L} - \frac{r_0}{L} \tag{3.17}$$

being a repository constant accounting for a zero strain energy at $\bar{\lambda}_i = 1$ (Alastrué et al., 2007). Notice that in both cases fibers are assumed not to bear any load under compression.

3.4 Fitting material parameters and comparison

The strain energy functions in Section (3.3) was used to fit experimental curves of simple tension tests carried out on human coronary arteries (Holzapfel et al., 2005). Data coming from thirteen individuals for media and adventitia layers were fit. To be specific, experiments on samples along the circumferential and longitudinal directions of the cylindrical frame $\{\mathbf{e}_{\theta,z,r}\}$ were considered. A least-square scheme was used to minimise the functional

$$\chi^2 = \sum_{j=1}^{p}\left[\left[\sigma_{\theta\theta} - \sigma_{\theta\theta}^{\Psi}\right]_j^2 + \left[\sigma_{zz} - \sigma_{zz}^{\Psi}\right]_j^2\right], \tag{3.18}$$

with p the number of experimental measures, $\sigma_{\theta\theta}$ and σ_{zz} the Cauchy stress data obtained from the tests, and $\sigma_{\theta\theta}^{\Psi}$ and σ_{zz}^{Ψ} representing the Cauchy stresses obtained from (3.35) as $\sigma^{\Psi} = J^{-1}\,\tau^{\Psi}$.

Nevertheless, in the case of the Bingham distribution, a single ODF was used to reproduce the curves where two are needed in the von Mises distribution, for which the eigenvalues of the $\mathbf{Z}$ matrix – namely, $\kappa_{1,2,3}$ – were assumed to be in the interval $[0,\,\infty)$ representing the concentration parameters associated to the radial, the longitudinal and the circumferential directions, respectively. Then, following experimental evidences (Rhodin, 1980), the preferential orientation of the microfiber were assumed to be contained in the plane formed by vectors $\mathbf{e}_\theta$ and $\mathbf{e}_z$ by fixing $\kappa_1 = 0$.

A quasi-Newton minimization algorithm was used to minimize Eq. (3.18). The normalized root mean square error

$$\varepsilon = \frac{1}{\mu}\,\sqrt{\chi^2/[p-q]}\,, \tag{3.19}$$

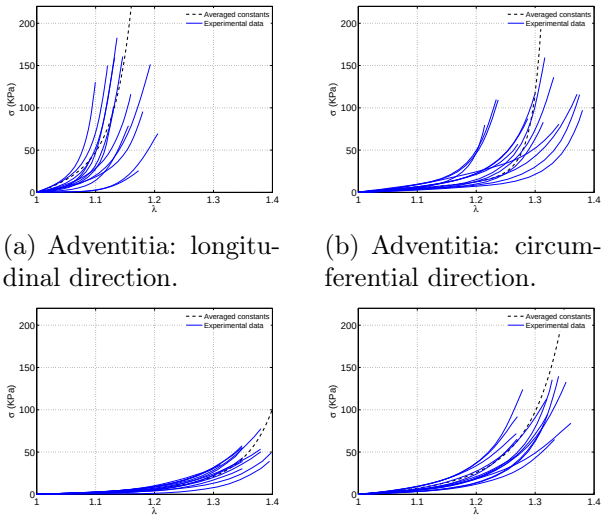

(a) Adventitia: longitudinal direction.

(b) Adventitia: circumferential direction.

(c) Media: longitudinal direction.

(d) Media: circumferential direction.

Figure 3.3: Exponential fiber behavior: simulation results of uniaxial tension tests and experimental data.

was used as a measure of the quality of the approximated set of parameters, where q is the number of parameters to be identified so that $p-q$ is the number of degrees of freedom, and μ represents the mean stress defined as

$$\mu = \frac{1}{p} \sum_{j=1}^{p} \left[\sigma_{\theta\theta} + \sigma_{zz}\right]_j . \tag{3.20}$$

Following Alastrué et al. (2009a), the deformation gradient tensors causing the stress-strain curves reported by Holzapfel et al. (2005) were assumed to correspond to pure shear deformations, namely $\mathbf{F} = \lambda\, \mathbf{e}_\theta \otimes \mathbf{e}_\theta + \lambda^{-1}\, \mathbf{e}_z \otimes \mathbf{e}_z + \mathbf{e}_r \otimes \mathbf{e}_r$ and $\mathbf{F} = \lambda^{-1}\mathbf{e}_\theta \otimes \mathbf{e}_\theta + \lambda \mathbf{e}_z \otimes \mathbf{e}_z + \mathbf{e}_r \otimes \mathbf{e}_r$ for the circumferential and longitudinal samples, respectively.

The obtained sets of constant for each of the individuals together with the averaged values and the standard deviation are collected, for the von Mises distribution, in Table 3.1 and 3.2 for the exponential micro-structural behavior (3.15). In Table 3.3 and 3.4 for the worm-like structural behavior in Eq. (3.16). The graphic representation is presented in Fig. 3.3 and Fig. 3.4. The mean and the standard deviation for the Bingham distribution are presented, in the same way, in Table 3.6 and Table 3.5.

Three-dimensional plots of the von Mises and Bingham ODF, for the identified parameters presented above are depicted in Figure 3.5 and Figure 3.6 respectively. Note the similar values and shapes of the ODFs rendered by the identified set of constants for both micro-structural behaviors. As it is seen in Fig. 3.5a and b and Fig. 3.6a and b, the fibers are preferentially oriented along the longitudinal direction in the adventitia layer, whereas its preferred orientation is along the circumferential direction in the medial layer, Fig. 3.5c and d and Fig. 3.6c and d.

Table 3.1: Material parameters identified for the adventitia layer based on exponential fiber behavior for the von Mises distribution: μ [kPa], k_1 [kPa], k_2 [-], b [-], ϑ [°], ε [-].

Specimen	μ	k_1	k_2	b	ϑ	ε
1	4.04	82.768	36.954	10.340	65.43	0.187
2	2.41	79.657	13.721	10.616	60.84	0.262
3	4.91	89.441	14.154	8.271	55.17	0.117
4	16.41	18.606	11.260	4.502	68.13	0.149
5	9.65	32.094	16.797	2.936	58.74	0.139
6	7.92	78.434	22.478	14.038	63.27	0.250
7	7.07	90.307	12.062	5.187	67.05	0.242
8	2.25	48.856	12.156	5.954	59.22	0.075
9	6.16	41.872	24.257	3.149	67.77	0.088
10	14.93	91.374	55.450	15.000	51.99	0.168
11	12.71	76.972	29.472	10.315	62.37	0.155
12	3.13	13.411	8.779	1.582	60.83	0.046
13	6.69	21.935	5.321	1.998	68.58	0.189
Mean	7.560	58.902	20.220	7.222	62.260	0.159
SD	4.658	30.071	13.795	4.528	5.165	0.067

Table 3.2: Material parameters identified for the medial layer based on exponential fiber behavior for the von Mises distribution: μ [kPa], k_1 [kPa], k_2 [-], b [-], ϑ [°], ε [-].

Specimen	μ	k_1	k_2	b	ϑ	ε
1	0.94	10.541	4.486	1.589	23.10	0.042
2	1.09	16.071	3.309	1.587	28.38	0.083
3	1.79	12.863	3.917	1.059	25.30	0.118
4	1.63	21.501	4.214	2.588	28.16	0.047
5	2.54	15.245	4.506	1.157	18.70	0.075
6	0.73	23.962	3.203	1.316	16.83	0.049
7	0.93	17.825	3.598	0.768	11.07	0.061
8	0.32	26.119	2.983	0.777	11.44	0.031
9	2.31	5.301	5.408	2.564	27.39	0.031
10	0.85	25.223	1.910	0.435	18.04	0.059
11	1.21	7.210	3.754	1.772	26.73	0.087
12	0.96	20.640	3.218	0.642	22.55	0.032
13	1.19	19.013	4.602	2.596	24.42	0.059
Mean	1.268	17.040	3.778	1.451	21.700	0.056
SD	0.634	6.664	0.894	0.755	5.996	0.026

Table 3.3: Material parameters identified for the adventitia layer based on worm-like-chain fiber behavior for the von Mises distribution: μ [kPa], B [kPa], r_0 [mm], L [mm], b [-], ϑ [°], ε [-].

Specimen	μ	B	r_0	L	b	ϑ	ε
1	4.04	3.441	0.527	0.677	4.311	65.43	0.337
2	2.41	3.741	0.100	0.139	2.812	74.36	0.351
3	4.91	2.344	0.135	0.179	2.244	67.43	0.190
4	16.41	1.360	0.597	0.813	2.289	74.89	0.240
5	9.65	0.843	0.390	0.491	2.075	58.74	0.245
6	7.92	5.277	1.089	1.512	3.049	77.33	0.415
7	7.07	4.221	0.100	0.135	2.209	81.95	0.317
8	2.25	1.886	0.512	0.681	2.404	72.38	0.238
9	6.16	0.664	0.233	0.287	1.564	82.83	0.187
10	14.93	1.520	0.251	0.312	4.010	58.74	0.333
11	12.71	2.696	0.100	0.130	2.840	76.23	0.302
12	3.13	0.757	0.766	1.027	0.623	55.14	0.159
13	6.69	1.589	0.581	0.817	1.069	82.12	0.325
Mean	7.560	2.334	0.414	0.554	2.423	71.352	0.281
SD	4.658	1.455	0.302	0.419	1.033	9.458	0.076

Table 3.4: Material parameters identified for the medial layer based on worm-like-chain fiber behavior for the von Mises distribution: μ [kPa], B [kPa], r_0 [mm], L [mm], b [-], ϑ [°], ε [-].

Specimen	μ	B	r_0	L	b	ϑ	ε
1	0.940	0.561	0.968	1.340	1.601	21.0	0.059
2	1.090	1.042	1.077	1.538	1.484	25.8	0.161
3	1.790	1.013	1.190	1.695	0.945	23.0	0.212
4	1.630	0.962	0.952	1.314	2.440	25.6	0.109
5	2.540	0.852	1.104	1.534	1.101	17.0	0.162
6	0.730	1.096	0.912	1.277	1.494	18.7	0.061
7	0.930	0.865	1.077	1.506	0.834	12.3	0.050
8	0.320	1.411	0.972	1.380	0.805	10.4	0.062
9	2.310	0.570	1.023	1.439	2.748	24.9	0.224
10	0.850	1.824	1.145	1.700	0.440	16.4	0.099
11	1.210	0.474	1.158	1.637	2.486	29.7	0.145
12	0.960	1.263	1.012	1.442	0.660	20.5	0.080
13	1.190	1.310	0.992	1.395	2.393	22.2	0.199
Mean	1.268	1.019	1.045	1.477	1.495	20.576	0.125
SD	0.634	0.378	0.087	0.139	0.787	5.544	0.062

Table 3.5: Material parameters identified based on exponential fiber behavior for the Bingham distribution.

Layer	-	μ [kPa]	k_1 [kPa]	k_2 [-]	κ_2 [-]	κ_3 [-]	ε [-]
Adventitia	Mean	7.560	55.176	14.755	63.534	57.334	0.186
	SD	4.658	29.106	8.638	16.301	14.355	0.072
Media	Mean	1.268	19.622	3.437	61.606	63.416	0.072
	SD	0.634	7.867	0.810	19.420	19.635	0.029

Table 3.6: Material parameters identified based on worm-like-chain fiber behavior for the Bingham distribution.

Layer	-	μ [kPa]	B [kPa]	r_0 [mm]	L [mm]	κ_2 [-]	κ_3 [-]	ε [-]
Adventitia	Mean	7.560	3.622	0.752	1.000	61.210	57.830	0.273
-	SD	4.658	2.529	0.425	0.564	15.142	15.505	0.079
Media	Mean	1.268	1.406	1.072	1.532	56.809	58.699	0.117
-	SD	0.634	0.527	0.496	0.705	17.311	17.911	0.058

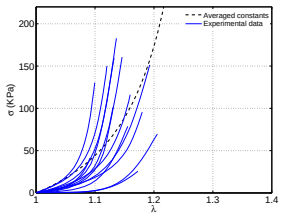

(a) Adventitia: longitudinal direction.

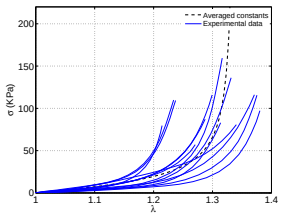

(b) Adventitia: circumferential direction.

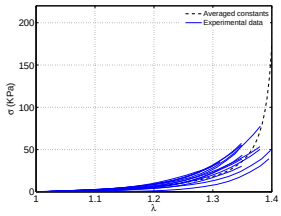

(c) Media: longitudinal direction.

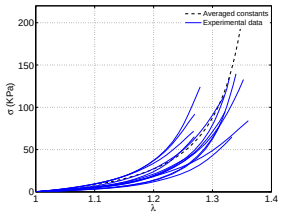

(d) Media: circumferential direction.

Figure 3.4: Worm-like chain fiber behavior: simulation results of uniaxial tension tests and experimental data.

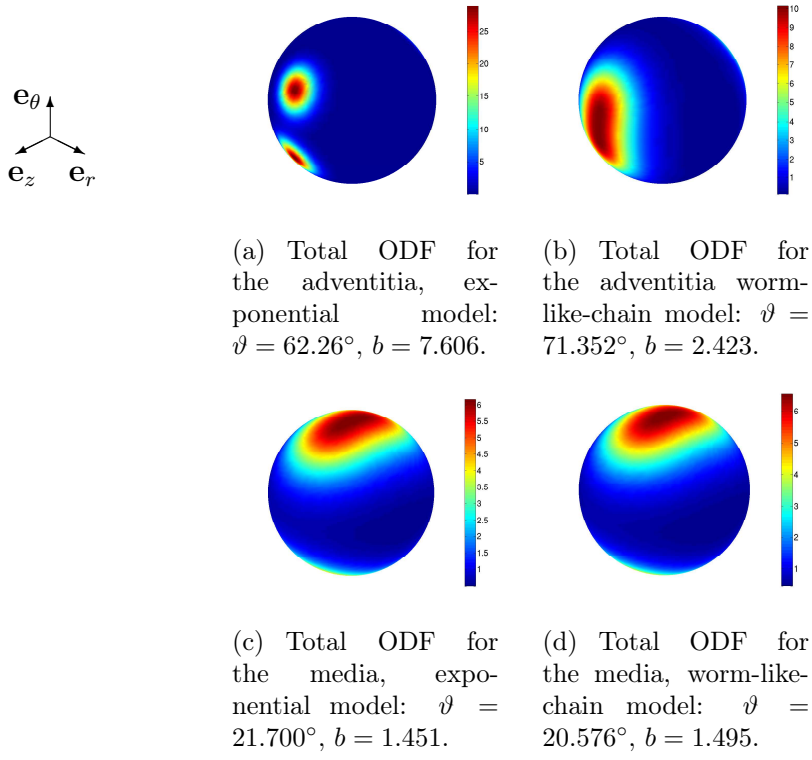

(a) Total ODF for the adventitia, exponential model: $\vartheta = 62.26°$, $b = 7.606$.

(b) Total ODF for the adventitia worm-like-chain model: $\vartheta = 71.352°$, $b = 2.423$.

(c) Total ODF for the media, exponential model: $\vartheta = 21.700°$, $b = 1.451$.

(d) Total ODF for the media, worm-like-chain model: $\vartheta = 20.576°$, $b = 1.495$.

Figure 3.5: Representation of the von Mises ODF, $\rho_{tot} = \rho_1 + \rho_2$, for the identified averaged values b and ϑ – the angle ϑ for the purpose of visualization being referred to the vertical direction.

The von Mises and the Bingham statistical functions has been considered in this work for the incorporation of anisotropy to a hyperelastic micro-sphere-based constitutive law with application to the modeling of the vascular tissue. The obtained results show a good agreement with the experimental data, with values of the normalized root means squared error very similar between them.

Homogeneous deformation states were reproduced in order to compare both the von Mises and Bingham ODFs. An equivalent response is attached for the two ODFs for the uniaxial tests (Fig. 3.7(a) and 3.7(b) and Fig. 3.8(a) and 3.8(b)). For the equi-biaxial tests, a good correlations also found in all cases except for the exponential fiber behavior in the adventitia layer Fig. (3.7(c) and (d) and Fig. 3.8(c) and (d)). In view of these results, it is worth noting that the use of the Bingham distribution allowed getting similar results with a single family of fibers compared with the two helically oriented families of fibers – or rather preferential orientations – modeled by means of the von Mises ODF. This fact, which is crucial in the reduction of the computation associated the numerical calculation of the macroscopic stress, points out the feasibility of the Bingham distribution to include anisotropy in the micro-sphere based models.

Nevertheless, some simplifications have been taken for the obtaining of the results here presented. The most important one regards the use of the eigenvalues

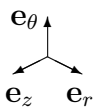

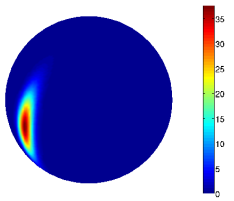

(a) Adventitia, exponential model: $\kappa_2 = 63.53$, $\kappa_3 = 57.33$.

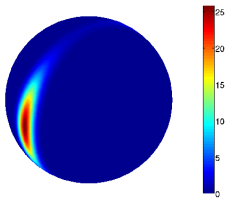

(b) Adventitia, worm-like-chain model: $\kappa_2 = 61.21$, $\kappa_3 = 57.83$.

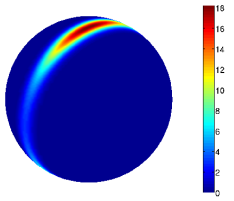

(c) Media, exponential model: $\kappa_2 = 61.61$, $\kappa_3 = 63.42$.

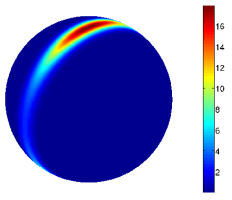

(d) Media, worm-like-chain model: $\kappa_2 = 56.81$, $\kappa_3 = 58.70$.

Figure 3.6: Representation of the Bingham ODF for the identified averaged values κ_2 and κ_3 – the circumferential direction is referred to the $\mathbf{e}_z$ direction, whereas $\mathbf{e}_x$ corresponds to the longitudinal one.

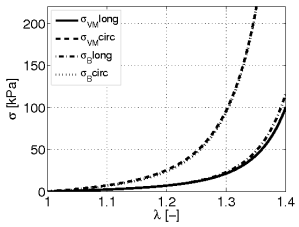

(a) Uniaxial test, media layer.

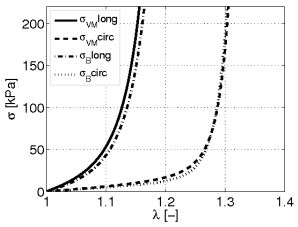

(b) Uniaxial test, adventitia layer.

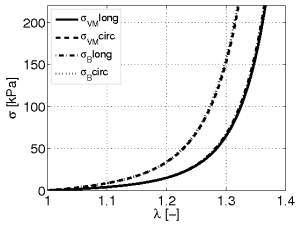

(c) Biaxial test, media layer.

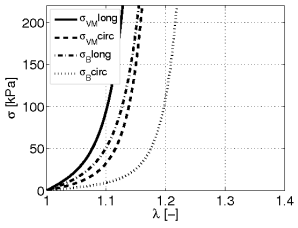

(d) Biaxial test, adventitia layer.

Figure 3.7: Comparison between Von Misses and Bingham ODF for exponential fiber behaviour (Media and adventitia layer).

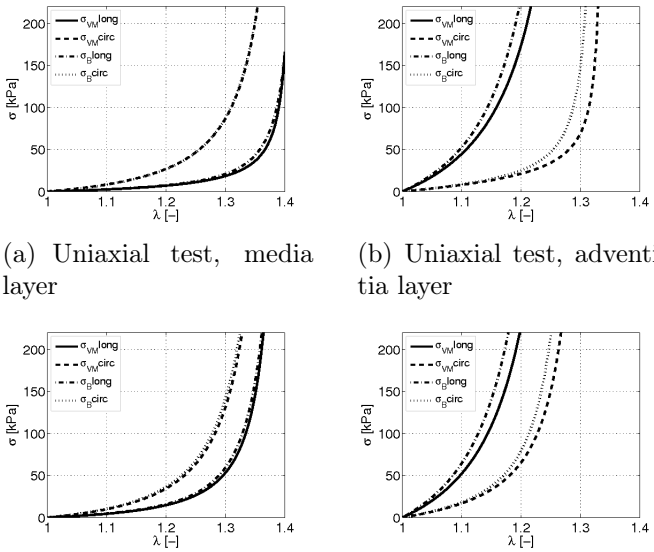

(a) Uniaxial test, media layer

(b) Uniaxial test, adventitia layer

(c) Biaxial test, media layer

(d) Biaxial test, adventitia layer

Figure 3.8: Comparison between Von Misses and Bingham ODF for eight-chain model fiber behaviour (media and adventitia layer).

of **Z** as additional identification parameters for macroscopic stress-stretch curves. On the contrary, those parameters should by identified from measurements at the micro-structural level (Landuyt, 2006). Moreover, the eigenvectors of Z were assumed coincident to the vectors $\mathbf{e}_\theta$, $\mathbf{e}_\theta$ and $\mathbf{e}_z$, when the actual orientation at the micro-structural level can follow a more random distribution. However, this simplification has a strong experimental basis, since most of the histological studies show that most of the fibers are comprised in that plane (Rhodin, 1980). Moreover, the contribution of the isotropic neo-Hookean term constant μ was fixed to value obtained by Holzapfel et al. (2005), which might influence the results of the fittings. Nevertheless, it has been reported that the isotropic contribution to the macroscopic stress is only relevant up to certain value of stretch, from which collagen fibers bear most of the load (Holzapfel et al., 2000). In addition, fixing μ allowed us to establish direct comparisons with the values reported in Alastrué et al. (2009a). Finally, the deformation gradient causing the stress-stretch curves was assumed to correspond to a uniaxial and equibiaxial tension with incompressibility constraint. Other deformation fields fulfilling this requirement might have been used, though previous studies show that the obtained constants are barely dependent on the used deformation field (Alastrué et al., 2009a).

3.5 Damage model

The structural model used in this work is able to describe the softening of the material in a large strain non-lineal framework using the concept of internal variables

to describe situations with irreversible effects. To deal with behaviors far from the softening (i.e., fracture) other techniques like cohesive models should be performed although this is out of the scope of the present work.

The damage model uses the concept of internal variables, which provides a general description of materials involving irreversible effects and therefore, must fulfill the Clausius-Planck inequality, expressed in his material form and without thermal effects as $\mathcal{D} = -\dot{\Psi} + \mathbf{P} : \dot{\mathbf{F}} \geq 0$ where $\mathcal{D}$ is the internal dissipation and $\dot{(\cdot)}$ the material time derivative.

Since the volumetric part is related with the water content in soft biological tissue, is well established that damage is just affected by the isochoric part. Using the previous splitted form of the free energy,

$$\Psi_{iso}(\bar{I}_1) = [1 - D_M]\Psi_{0,\text{iso}}(\bar{I}_1) \tag{3.21}$$

$$\Psi_{ani} \approx \sum_{j=1}^{N} \left[\sum_{i=1}^{m} n\rho_i w^i [1 - D_i]\psi_0(\overline{\lambda}_i) \right] \tag{3.22}$$

where $\mathrm{g} = [1 - D]$ is a reduction factor with $D \in [0, 1]$ a monotonically increasing damage internal variable (Simo, 1987). D_M and D_i are the damage variable for matrix and for each integration direction respectively and $\Psi_{0,\text{iso}}(\bar{I}_1)$ and $\psi_0(\overline{\lambda}_i)$ the effective strain energy function of the hypothetical undamaged matrix and fibers respectively. From now on all the equations will be given for the isotropic and anisotropic part.

In order to fulfill the Clausius-Planck inequality, $\mathcal{D} = f\dot{D} \geq 0$ must be satisfied, with $f_{\mathrm{M}} = -\partial\Psi(\bar{I}_1)/\partial D \geq 0$ and $f_i = -\partial\psi(\overline{\lambda}_i)/\partial D_i \geq 0$ the thermodynamic forces for matrix and fibers respectively. The thermodynamic force f is conjugated to the internal variable D, so the process could be controlled by f instead of D. For more details see e.g. Simo (1987); Calvo et al. (2007). The damage evolution equations are given in the strain space, therefore, the free energy of the integration directions, are given just by $\overline{I}_1$ and the stretch ratio $\overline{\lambda}_i$ for matrix and fibrils respectively. The damage variable D is given by the irreversible equation of evolution $\Xi_M = \sqrt{2\Psi_0(\overline{I}_1(s))}$ and $\Xi_i = \sqrt{2\psi_0(\overline{\lambda}_i(s))}$ where $\overline{I}_1(s)$ the first invariant and $\overline{\lambda}_i(s)$ is the stretch ratio at pseudo-time $s \in \mathbb{R}^+$, $\Xi_M^* = \max_{s\epsilon(-\infty,t]}\sqrt{2\Psi_0(\overline{I}_1(s))}$ and $\Xi_i^* = \max_{s\epsilon(-\infty,t]}\sqrt{2\psi_0(\overline{\lambda}_i(s))}$ the maximum thermodynamic force achieved all over the load history. Then, the damage criterion in the strain space is given by the condition

$$\Phi_{\mathrm{M}}(\overline{I}_1(s), \Xi_{s,\mathrm{M}}^*) = \sqrt{2\Psi_0(\overline{I}_1(s))} - \Xi_{\mathrm{M}}^* \leq 0 \tag{3.23}$$

$$\Phi_i(\overline{\lambda}_i(s), \Xi_{s,i}^*) = \sqrt{2\psi_0(\overline{\lambda}_i(s))} - \Xi_i^* \leq 0 \tag{3.24}$$

which leads to two different situations. If $\Phi < 0$, no damage occurs and $\Phi = 0$ defines the damage surface. Note that $\Phi > 0$ is an impossible situation. The

update of this surface occurs when the free energy of a determined material point or fiber goes up over Ξ^*. Defining the normal of the damage surface in that space as $\mathbf{N}_M = \partial_{\mathbf{C}}\phi_M$ and $N_i = \partial_{\lambda_i}\phi_i$ the following situation may occur

$$\Phi_{\mathrm{M}} \leq 0 \text{and} \begin{cases} \mathbf{N}_{\mathrm{M}} : \dot{\overline{\mathbf{C}}} < 0 \\ \mathbf{N}_{\mathrm{M}} : \dot{\overline{\mathbf{C}}} = 0 \\ \mathbf{N}_{\mathrm{M}} : \dot{\overline{\mathbf{C}}} > 0 \end{cases} \tag{3.25}$$

$$\Phi_i \leq 0 \text{and} \begin{cases} N_i \cdot \dot{\overline{\lambda}}_i < 0 \\ N_i \cdot \dot{\overline{\lambda}}_i = 0 \\ N_i \cdot \dot{\overline{\lambda}}_i > 0 \end{cases} \tag{3.26}$$

which correspond, taken terminology from plasticity (Simo & Hughes, 1998), to an unloading, neutral loading and loading states respectively. The last equation needed in order to a complete definition of the model is the irreversible rate equation (3.27) and (3.28) of the damage variable D

$$\frac{\mathrm{d}D_M}{dt} = \begin{cases} h_M(\Xi_M)\dot{\Xi}_M \text{ if } \Phi_M = 0 \ \& \ \mathbf{N}_M : \dot{\overline{\mathbf{C}}} > 0 \\ 0 \text{ otherwise} \end{cases} \tag{3.27}$$

$$\frac{\mathrm{d}D_i}{dt} = \begin{cases} h_i(\Xi_i)\dot{\Xi}_i \text{ if } \Phi_i = 0 \ \& \ N_M : \dot{\overline{\lambda}}_i > 0 \\ 0 \text{ otherwise} \end{cases} \tag{3.28}$$

where $h_M(\Xi_M) = dD_M/d\Xi_M = -dg_M/d\Xi_M$ and $h_i(\Xi_i) = dD_i/d\Xi_i = -dg_i/d\Xi_i$ are the functions that characterize the damage evolution in the material. Finally, it is just missing the evolution of the maximum thermodynamic force, given as follow

$$\Xi^* = \begin{cases} \dot{f} = \mathbf{S}_0 : \frac{\dot{\mathbf{C}}}{2} \text{ if } \Phi = 0 \text{ and } \dot{f} > 0 \\ 0 \text{ otherway} \end{cases} \tag{3.29}$$

The integrity factor is defined for matrix and fibers as

$$g_M = [1 - D_{\mathrm{M}}] = \frac{1}{[1 + \exp[a_{\mathrm{M}}[\Xi_{\mathrm{M}} - c_{\mathrm{M}}]]]} \tag{3.30}$$

$$g_i = [1 - D_{\mathrm{i}}] = \frac{1}{[1 + \exp[a_{\mathrm{i}}[\Xi_{\mathrm{i}} - c_{\mathrm{i}}]]]} \tag{3.31}$$

where parameter a is used for define the slope while c measure the center of the function Fig. 3.5. The Kirchoff stress tensor $\boldsymbol{\tau}$ and the material elastic tensor, can be expressed for the isochoric part of the extra cellular matrix as

$$\boldsymbol{\tau}_{\mathrm{M}} = g_{\mathrm{M}}\boldsymbol{\tau}_{0\mathrm{M}} \tag{3.32}$$

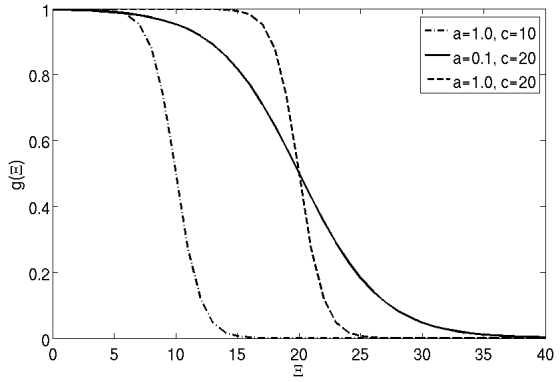

Figure 3.9: Shape of the integrity factor g for different parameters.

Algorithm 1 Implementation of an affine-stretch micro-sphere model with damage.

1. Get the initial data of integrity factors $\{g^i\}_{i=1...m}$ of the m integration directions as well its orientation vectors r^i and weights w^i.
2. Passed $\mathbf{F}$ to as a given data at the time t_{n+1} , calculate $\overline{\mathbf{F}}$, and compute the spatial integration orientation vector $\bar{\mathbf{t}} = \overline{\mathbf{F}}.\mathbf{r}$ and the associated micro-stresses $\overline{\lambda}_i$.
3. Compute the free energy function given by Eq. 3.15 and Eq. 3.16. Note that it just takes positive values for $\overline{\lambda}_i > 1$.
4. Compute integrity factor as follow: If $\psi^i_j(\overline{\lambda}_i)_{t_{n+1}} > \psi^i_j(\overline{\lambda}_i)_{t_n}$then compute $g_{t_{n+1}}$ and its derivatives with Eq. 3.30 and 3.31 else $g_{t_{n+1}} = g_{t_n}$.
5. Get micro-stresses and micro-elastic tensor of each fiber and get the macroscopic quantities through Equations 3.4 and 3.5.

$$\boldsymbol{\tau}_{0\mathrm{M}} = \mathbf{F}\left[J^{-2/3}DEV\left(2\frac{\partial\Psi_0(\overline{\mathbf{C}})}{\partial\overline{\mathbf{C}}}\right)\right]\mathbf{F}^T \tag{3.33}$$

$$\mathbf{c}_M = g_M\mathbf{c}_{M0} - g'_M\boldsymbol{\tau}_M \otimes \boldsymbol{\tau}_M \tag{3.34}$$

where $\boldsymbol{\tau}_{0M}$ and $\mathbf{c}_{0M}$ are the Kirchoff stress tensor and the material elastic tensors of the undamaged material (see Appendix A for details). And for the anisotropic part given as follows

$$\boldsymbol{\tau}^j_f = \sum_{i=1}^{m} g_i n\rho_i\psi'_i\overline{\lambda_i}^{-1}\bar{\mathbf{t}} \otimes \bar{\mathbf{t}} \tag{3.35}$$

$$\mathbf{c}^j_f = \textstyle\sum_{i=1}^{m} n\rho_j[g_i\psi''_i - g_i\psi'_i\overline{\lambda_i}^{-1} + g'_i\psi'^2_i]\overline{\lambda_i}^{-2}\bar{\mathbf{t}} \otimes \bar{\mathbf{t}} \otimes \bar{\mathbf{t}} \otimes \bar{\mathbf{t}} \tag{3.36}$$

where $\boldsymbol{\tau}^j_f$ and $\mathbf{c}^j_f$ are the above mentioned stress and elastic tensors for each family of fibers (see Appendix A for details).

4 Validation examples

The aim of this section is to show the performance and the physical mechanics involved in the presented model. Some examples that can describe the behavior of the model on very different situations are carried out. A brick and a thin plate with a hole in the middle have been investigated. The examples have been implemented in a finite element code ABAQUS by an user subroutine UMAT, in order to a later simulation of a real clinical application. All the following simulations have been modeled with a von Mises distribution and the exponential approach. The developed sensitivity analysis response to the knowledge that, several situations can be found in different soft tissues and, blood vessels in particular. In all these examples only fiber failure is considered in order to a better appreciation of the spreading damage over the unit sphere.

4.1 A displacement driven brick example

Some analysis have been carried out in order to investigate the influence of the damage parameters over the micro-sphere. The boundary conditions imposed over the brick correspond to an uniaxial test with a deformation gradient $\mathbf{F} = 1/\sqrt{\lambda}\mathbf{e}_x \otimes \mathbf{e}_x + 1/\sqrt{\lambda}\mathbf{e}_y \otimes \mathbf{e}_y + \lambda\mathbf{e}_z \otimes \mathbf{e}_z$ (Ogden, 1996). These simulations have been carried out up to $\lambda = 3$ (200% in $\mathbf{e}_z$ direction). Table 4.1 presents the different set of parameters established for each case and Fig. 3.1 capture in a graphic way its effect in the macroscopic behavior of the material.

	k_1[kpa]	k_2[-]	a[-]	c[kpa]	b[-]
Set1	100	1	1	50	1
Set2	100	1	0.1	50	1
Set3	100	1	1	30	1
Set4	100	1	1	50	10

Table 4.1: Parameters sets for the driven displacement uniaxial test

Variation of parameter a. As was shown in Fig. 3.5 the parameter a controls

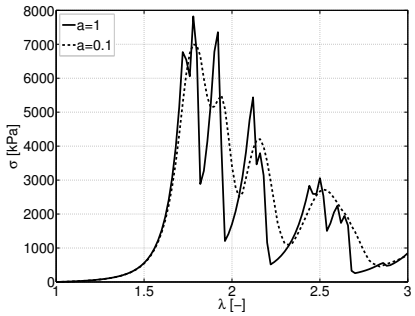

(a) Stress in $\mathbf{e}_z$ direction for Set1 and Set2.

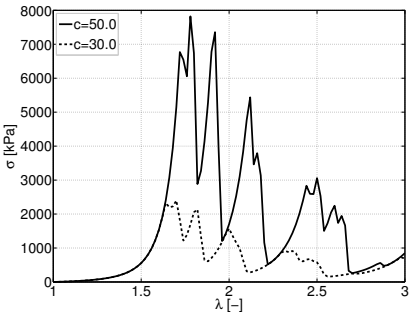

(b) Stress in $\mathbf{e}_z$ direction for Set1 and Set3.

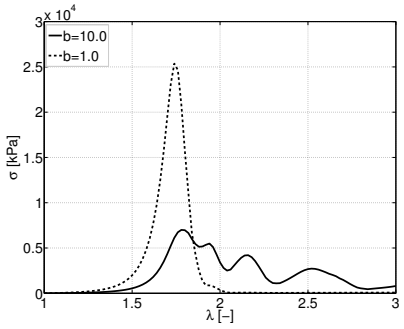

(c) Stress in $\mathbf{e}_z$ direction for Set2 and Set4.

Figure 4.1: Stress versus stretch in the loading direction. A variation of the damage parameters a and c, and b was perform. The defaults parameters are $k_1 = 100\,[KPa]$, $k_2 = 1$, $b = 1$, $a = 1$ and $c = 50$. **(a)** results for variation of a, **(b)** of c and **(c)** of b.

the evolution of the damage showing that damage evolves faster when a increases. The evolution of the stress over the stretching range is presented in Fig. 4.1a. A smoother response for $a = 0.1$ respect to the $a = 1.0$ case can be observed.

Variation of parameter c. The material parameter c represent the value of the energy density function at which the damage is a 50%. The lower the value of c the lower the value of stress achieved due to the sooner failure of the fibers. This fact is captured in Fig. 4.1b when c=30 curve presents a lower stress than the c=50 one.

Variation of parameter b. Fig. 4.1c shows the influence of b in the model. High concentrations of the fibers cause a faster failure of the material.As soon as any integration direction that are in the influence of the statistical distribution fail no other fibrils exits to works.

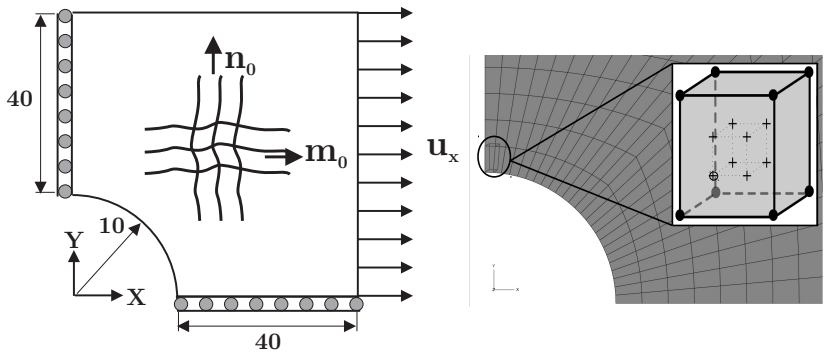

(a) Boundary conditions.

(b) Finite element mesh and integration point used for plotting purpose

Figure 4.2: Geometry and mesh for the thin perforated plate

4.2 Thin perforated plate

It is well know that a thin perforated plate is a critical case to check convergence and results in plasticity and damage models (Miehe, 1995; Neto et al., 1998). On this way, different sets of parameters were analyzed in this geometry. The model consist of a eight part of the whole geometry applying symmetry conditions (symmetry on the three planes) and pulling on $\mathbf{e}_x$ direction 15 mm, as shown Fig. 4.2a. Moreover, in order to get and control micro-stresses and micro-damage in the model, a stereographic projection has been performed (see Miehe et al. (2004); Alastrué et al. (2009a)) on the integration point capture in Fig. 4.2b at the element in the circle show in the same figure, of both the variables. The parameters selected and the convergence level is showed in Fig. 4.2.

	k_1 [kPa]	k_2 [-]	a [-]	c [kPa]	b [-]	%
Case 1	50	1	1	10	1	63.8
Case 2	50	1	1	5	1	100

Table 4.2: Parameters set for the driven displacement plate.

Fig. 4.3 and Fig. 4.4 show the results for Case 1 and Case 2 detailed in Fig. 4.2 respectively. Fig. 4.3a presents the stress map in the $\mathbf{e}_x$ axis at 50% of the analysis while Fig. 4.3d does it at the end. To get into the micro-structure results Fig. 4.3b and Fig. 4.3e show the integrity factor g at both strain levels while Fig. 4.3c and Fig. 4.3f present the X component of the stress tensor. Same structure of figures have been used for Case 2 and it are shown in Fig. 4.4.

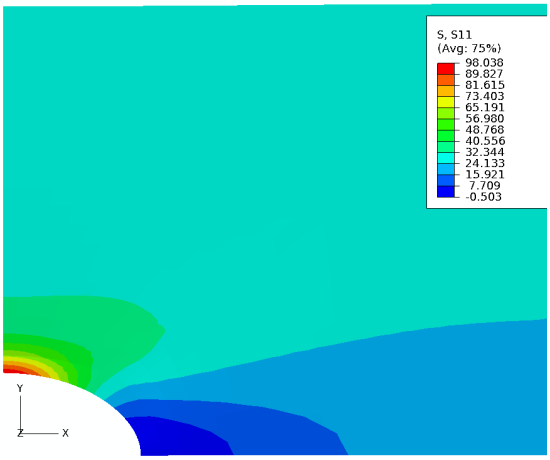

(a) Map of stress in X axis at 36.9%.

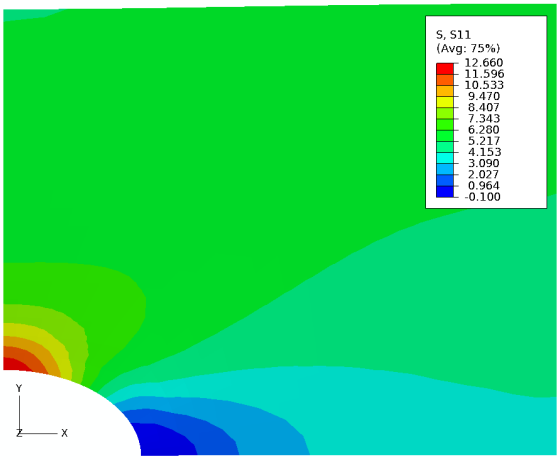

(a) Map of stress in X axis at 50%.

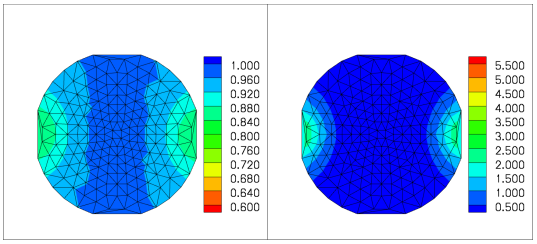

(b) g at 50% (c) S_x at 36.9%

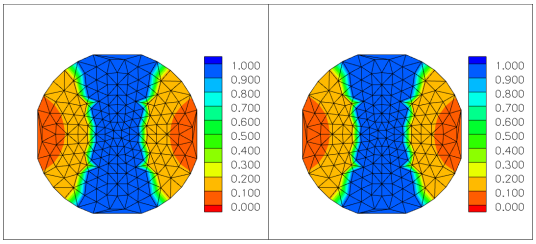

(b) g at 50% (c) S_x at 50%

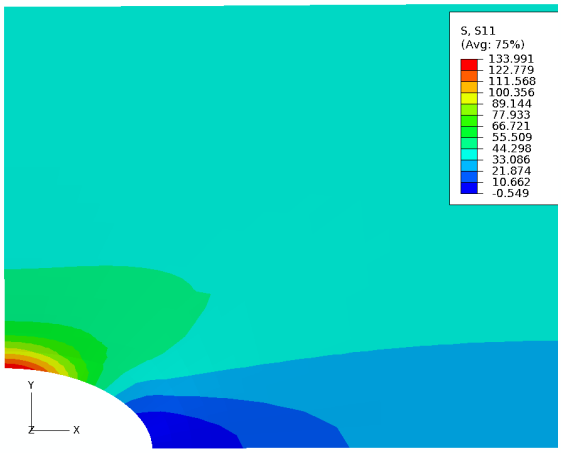

(d) Map of stress in X axis at 63.8%.

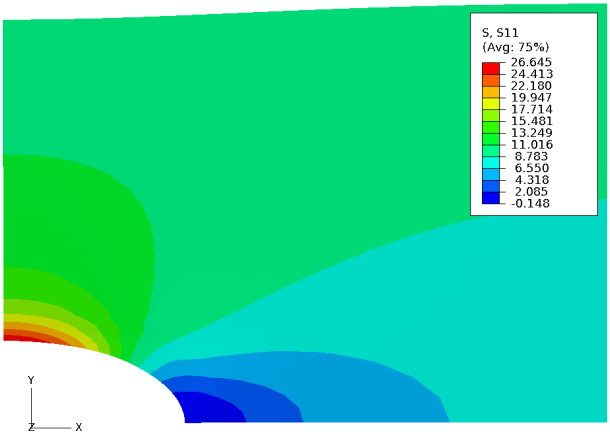

(d) Map of stress in X axis at 100%.

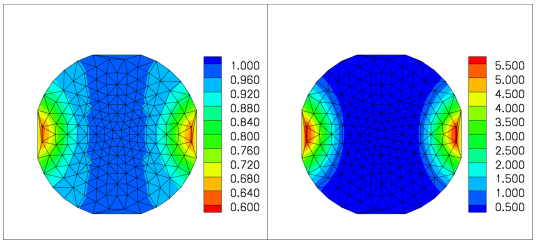

(e) [g at 63.8% (f) S_x at 63.8%

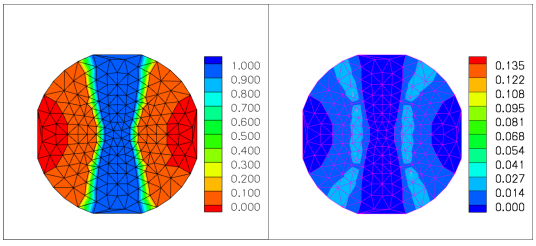

(e) g at 100% (f) S_x at 100%

Figure 4.3: Evolution of stress and $[1 - D]$ in the integration point for case 1.

Figure 4.4: Evolution of stress and $[1 - D]$ in the integration point for case 2.

Results present some important differences in both cases. Case 1 presents a tougher response, since the damage starts later than Case 2, and can not achieve total damage. At 50% of strain Case 1 present a maximum integrity factor of 0.84 and at the end reaches 0.6 in just the integration directions more alignment with $\mathbf{e}_x$ axis (note that when g increase, the damage D decrease). Case 2, with a sooner starting damage showed a value of 0.1 at the 50% and with a spreader distribution and damage close to 1 is obtained at 100% of strain. It is worth noting the evolution of the stress over the stereographic projection. Fig. 4.4.b capture a situation where the fibers along the $\mathbf{e}_x$ axis present a higher value than the other ones (although lower than those achieved without damage). However, Fig. 4.4.e shows a circular crown-like shape caused by the total failure of those fibrils oriented along $\mathbf{e}_x$ axis. Moreover, the more strain is achieved the more movement of the crown towards the middle plane.

5

Clinical application example: Simulation of angioplasty

One of the aims of these models is the realistic simulation of clinical applications. Angioplasty is one of the most widely spread techniques in vascular surgery. Therefore, the study of the mechanical behavior of vessels in this situations is an important task, since this procedure can affect to the vessel integrity reducing its stiffness (Oktay, 1994). In order to assess this behavior, an angioplasty procedure was simulated using the above presented model. A pig aorta artery was experimentally tested to fit the elastic and damage material parameters which were used in the finite element simulations.

In the following section the material parameters of the constitutive behavior and the damage model are fitted using experimental data (Peña et al., 2010). The vessel sample were cut comprising a longitudinal and a circumferential strips in order to perform uniaxial tests, and a least-square iterative method, as discussed in Section 3.4, is used for the identification process. The fitting procedure was carried out in two steps, the first one to fit the elastic part (before damage) and the second one for the damage part, when the softening phenomenon has started.

The analytical stress expression above mentioned needs a deformation imposed to be calculated. In this approach have been considered incompressibility behavior with a deformation gradient tensor given by $\mathbf{F} = \lambda \mathbf{e}_\theta \otimes \mathbf{e}_\theta + \lambda^{-1} \mathbf{e}_z \otimes \mathbf{e}_z + \mathbf{e}_r \otimes \mathbf{e}_r$, considering strain in the direction of pulling ($\mathbf{e}_\theta$), for the circumferential sample, or $\mathbf{e}_z$ in longitudinal direction.

Following these assumptions, Fig. 5.1 shows the identified parameter for the experimental test performed by Peña et al. (2010).

The goal of this study is not the simulation of a rigorous clinical study with accurate. Instead of that, the objective is to show the applicability of the pre-

μ [KPa]	k_1 [KPa]	k_2 [-]	b[-]	a[-]	c[KPa]
1.051	246.99	0.9111.49	52.77	0.61	26.10

Table 5.1: Elastic and damage parameters for the uniaxial test.

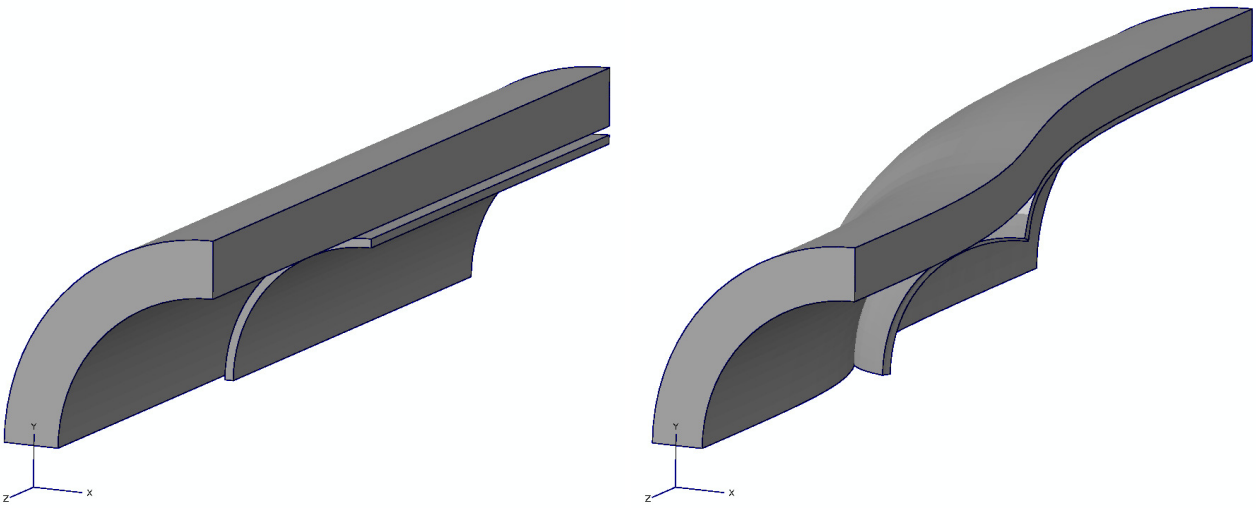

(a) Undeformed shape. (b) Deformed shape.

Figure 5.1: Undeformed and deformed shapes for the angioplasty simulation.

sented model to simulated the vessel behavior. The finite element simulation of the angioplasty was performed in a eight part of the model, applying symmetry conditions. The model consist of a 10 mm length sample with an external diameter $D_e = 5mm$ and an internal diameter $D_i = 3.7mm$ corresponding to coronary artery dimension. One only layer was considered since the well know intima, media and adventitia layers were not divided in the experimental test, so only information of the damage behavior of the whole artery was gathered. The artery is composed by an isotropic ground substance and two families of fibers, the angle respect to the circumferential direction show in Fig. 5.1 and the parameters shown in the same table. The geometry is discretized in 4788 hexahedrals elements. The balloon present the same dimension and material properties than in Alastrué et al. (2007); Gasser & Holzapfel (2007). The step loads are applied sequentially as follows: *(i)* Imposition of a initial deformation gradient as proposed by Rodriguez et al. (1994); Alastrué et al. (2007), *(ii)* Application of internal pressure of 13.3 kPa in the vessel supposing as the mean physiological pressure condition and *(iii)* Imposition of pressure to the internal face of the balloon following the curve shown in Alastrué et al. (2007) in order to reach the contact between vessel and balloon.

The undeformed and deformed shapes of the model are presented in Fig. 5.1a and 5.1b respectively. The maximal principal stress map on the artery at the end of the analysis is presented in Fig. 5.2a. The maximum stress, due to the one only layer simplification, is placed on the inner radius of the vessel. Some other authors (Alastrué et al., 2007), due to the incorporation of two different layers, observed different distribution of stress. Since the adventitia layer have a more circumferential distribution of the fiber, the maximal principal stress had higher values than the media layer. In order to present a mean value of the damage distribution over a given integration point depicted in Fig. 5.2b an averaged or

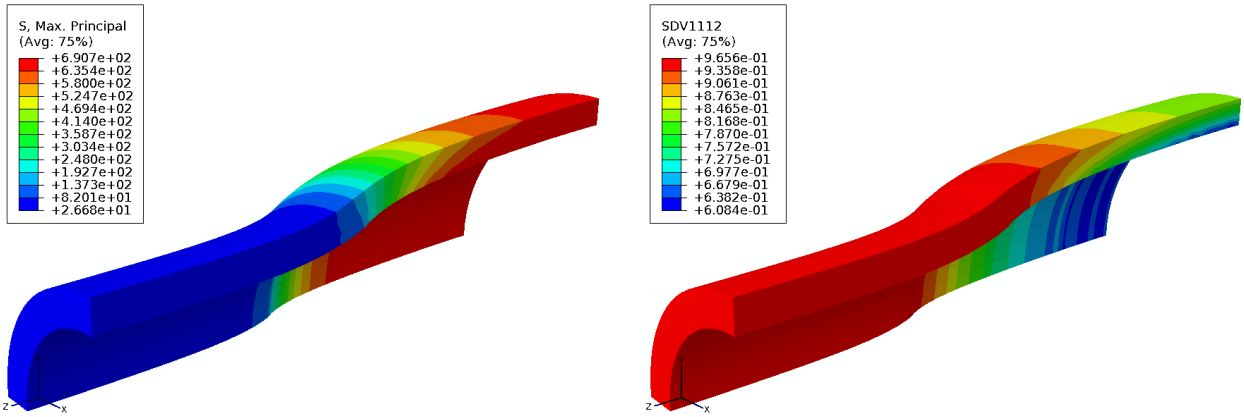

(a) Maximal principal stress map. (b) Integrated damage map.

Figure 5.2: State of the vessel at the end of the analysis

integrated value of the damage, defined as

$$D_{\text{ave}} = \int_{\mathbb{U}^2} \rho D dA \approx \sum_{i=1}^{m} \rho_i D_i w^i \tag{5.1}$$

According to the stress results, the highest damage value is localized on the inner radius. For a better visualization of the behavior of the vessel, Fig. 5.3 presents the the micro-structure stress at the end of the analysis for the undamaged case, Fig. 5.3a, and the damaged case, Fig. 5.3b. It is clearly appreciable the two family of fibers stress and the influence of the damage phenomenon. Fig. 5.4 presents the stress in the circumferential direction, showing that the vessel start to damage in the last increments of the analysis , observing a softening effect.

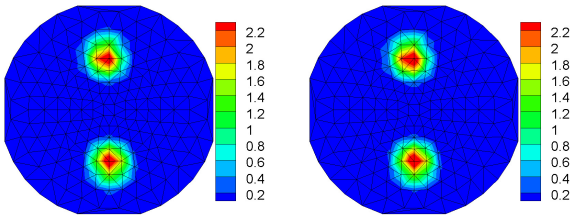

(a) Micro stress for the undamage vessel (b) Micro stresses for the damaged vessel

Figure 5.3: Micro-stresses for the undamaged and damaged model.

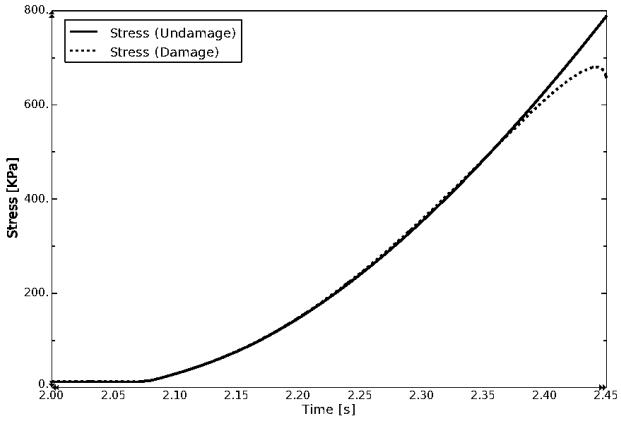

Figure 5.4: Maximum stress for circunferential direction for the damaged and undamaged model.

6 Conclusions

The main goal of this work was to present a formulation for a damage model within a micro-sphere-based approach in order to a better characterization of this phenomenon in biological soft tissues. The model was formulated in a hyperelastic framework, using the splitting of the free Helmholtz energy density function into a volumetric and an isochoric part, which was split again into a isotropic part, associated with the extracellular matrix and an anisotropic part which meanly deals with the distribution of the collagen fibers. To this end, the free energy associated to the fibrils was expressed in terms of the stretch rate instead of the widely used invariant form. Therefore, in the framework of a multi-scale model an homogenization scheme was required to move from the micro to the macro level. The micro-sphere-based approach was used to this purpose, carrying out a numerical integration of the stress and elastic tensors over the surface of the unit sphere. Moreover, within this approach, a phenomenological damage model, previously developed for unidirectional families of fibers was incorporated in the micro-sphere-based approach. Previous works (Alastrué et al., 2009a) studied different discretization for the numerical integration, leading to 368 discretization as a optimum value in order to avoid a lack of accuracy in the results.

The model was implemented in a commercial finite element code (ABAQUS) through a material subroutine (UMAT) and checked with different sets of material parameters and geometries, in particular a brick and a perforated plate, since it is well known that damage models present convergence problems, in particular in driven force problems. In fact, for the uniform strain example, convergence was achieved for all the sets of parameters, while it was not the case for the plate due to localization problems. The results reported in the brick case showed some important characteristics of the proposed model. As far as the damage parameters concern, the parameter a (related on how fast the evolution of the damage is) showed that the lower the parameter the smoother the evolution on the stress; while c (energy level at which the damage starts) showed that the lower the value of c the lower the stress achieved. The higher the concentration parameter the higher the maximum value of stress and the lower the point of total failure. This point will be discuss later. In order to obtain the behavior in a non homogeneous deformation

state in the thin perforated plate, other two sets of parameters was investigated. Classical convergence problems due to localization and loss of ellipticity appear and therefore, depending on the chosen parameters the convergence rate increases or decreases. Apart from this issue, the result showed high level of damage and stress concentration around the hole. Regarding the angioplasty simulation, in spite of lack in experimental data and the mono-layer simplification, it demonstrates the capability of the model to simulate clinical applications, including damage phenomenon, with higher level of information. Although the fitting scheme is still a handicap and some numerical integration improvements could be done in the future, these micro-structure models present a chance in order to know what is happening inside the material.

Therefore, the present model has some important limitations. The most important one is the undetermined parameter fitting problem. The idea followed in this work to fit the experimental data with a least-square minimization algorithm being aware that the achieved parameter sets are not the unique ones able to reproduce the material behavior. Although some restrictions were applied in order to reduce the solution field, the authors couldn't get a unique solution. The best way to reduce this underdetermination would be a direct measurement of the micro-structural parameters, through experimental tests. Other limitation, which avoid an ideal development of the model is the problem coming from the mismatch between the distribution of the concentration parameter and the integration directions. In cases with high concentration distributions, there are many of the integration direction that are not used in a optimum way, since match whit position where no fibrils exits. Alastrué et al. (2009b) worked about this issue and will be a priority line of future work. The last important problem arises from the well know lost of ellipticity of the problem on damage simulations. Developing of a model that overcomes these localization problems (Steinmann, 1999) is left for future work.

In spite of these limitations, the one dimensional character of the constitutive equation applied at the micro-level offers huge possibilities, due to the simplicity and the possibility of incorporation of other micro-variables. Menzel & Waffenschmidt (2009) have reported some works related to remodeling processes and the works Göktepe & Miehe (2005); Miehe & Göktepe (2005) developed some inelastic models on the micro-sphere framework for isotropic materials. Moreover, the incorporation of the von Mises or the Bingham ODF could allow, in a really physical way, the development of some remodeling models such as those reported by Kuhl et al. (2005) or Menzel et al. (2007), whose preferential orientation direction can evolve during the simulation. This probabilistic function may be used coupled with growing and remodeling models, accounting for the mass transference and also reorientation of the fibers that could be modeled, for example, by modification of the ODF of the fibers. Therefore, it seems clear that the research field including these micro structure models is extremely wide and can be improve the constitutive models of soft biological tissue.

As far as the comparison between the two ODF studied, the presented results show the capability of the presented micro-sphere models together with the Bing-

ham or the von Mises distribution to reproduce the mechanical behavior of soft biological tissues, in particular, of the human coronary artery.

In conclusion, the model presents a multi scale model capable to reproduce the softening behavior of biological soft tissues in general and blood vessels in particular. The present model uses a micro-structural approach, which represent a clear advantage over other phenomenological damage models, since almost all of them treat fibers as a unidimensional material that can not capture the progressive failure of the fibrils bundle.

A

Obtention of stress and elasticity tensors

In order to obtain the useful equation of the stress tensor some manipulations have to been performed. Starting up from

$$\mathbf{P} = \frac{\partial \Psi(\mathbf{F})}{\partial \mathbf{F}} = 2\mathbf{F} \cdot \frac{\partial \Psi(\mathbf{C})}{\partial \mathbf{C}} = \mathbf{F} \cdot \mathbf{S} \tag{A.1}$$

and

$$\mathbf{S} = \frac{\partial \Psi_{\text{vol}}(J)}{\partial \mathbf{C}} + \frac{\partial \Psi_{\text{ich}}(\overline{\mathbf{C}})}{\partial \mathbf{C}} = \mathbf{S}_{\text{vol}} + \mathbf{S}_{\text{ich}} \tag{A.2}$$

$$\boldsymbol{\tau} = J\boldsymbol{\sigma} = 2J^{-1}\mathbf{F} \cdot [\mathbf{S}_{\text{vol}} + \mathbf{S}_{\text{ich}}] \cdot \mathbf{F}^T \tag{A.3}$$

using a decoupled form and splitting the isochoric part in a isotropic and anisotropic part and after some mathematical manipulations

$$\boldsymbol{\tau}_{\text{vol}} = Jp\mathbf{I} \quad \text{where} \quad p = \frac{\partial \Psi_{\text{vol}}}{\partial J} \tag{A.4}$$

For the isochoric part

$$\mathbf{S}_{\text{ich}} = \frac{\partial \Psi_{\text{ich}}(\overline{\boldsymbol{C}})}{\partial \mathbf{C}} : \frac{\partial \overline{\mathbf{C}}}{\partial \overline{\mathbf{C}}} = J^{-2/3}\mathbb{P} : \overline{\mathbf{S}} = J^{-2/3}DEV(\overline{\mathbf{S}}) \tag{A.5}$$

where $\mathbf{P}$ is a projection tensor with respect to the reference configuration

$$\mathbf{P} = \mathbf{I} - \frac{1}{3}\mathbf{C}^{-1} \otimes \mathbf{C} \tag{A.6}$$

which leads to, after some manipulations,

$$\boldsymbol{\tau}_{\text{iso}} = \mathbf{F} \cdot \mathbf{S}_{ich} \cdot \mathbf{F}^T = \mathbf{F}[J^{-2/3}DEV(\overline{\mathbf{S}})]\mathbf{F}^T = \overline{\mathbf{F}} \cdot DEV(\overline{\mathbf{S}}) \cdot \overline{\mathbf{F}}^T = dev(\overline{\boldsymbol{\tau}}_{iso}) \tag{A.7}$$

where

$$dev(\bullet) = [\bullet] - \frac{1}{3}[[\bullet] : \mathbf{I}]\mathbf{I} \tag{A.8}$$

$$\overline{\boldsymbol{\tau}}_{iso} = 2\mathbf{F} \cdot \frac{\partial \Psi_{iso}(\overline{\boldsymbol{C}})}{\partial \overline{\mathbf{C}}} \cdot \mathbf{F}^T \tag{A.9}$$

The expression (A.9) is usually written in terms of the invariants (Holzapfel, 2000). This approach will be used here to the isotropic part (A.10) but an expression in terms of the stretch rate will be used for the anisotropic part (A.11) due to the unidimensional character of the micro model.

$$\frac{\partial \Psi_{\mathrm{iso}}(\overline{\boldsymbol{C}})}{\partial \overline{\mathbf{C}}} = \frac{\partial \Psi_{\mathrm{iso}}(\bar{\mathrm{I}}_1)}{\partial \bar{\mathrm{I}}_1}\mathbf{I} \tag{A.10}$$

$$\frac{\partial \Psi_{\mathrm{ani}}(\overline{\boldsymbol{C}})}{\partial \overline{\mathbf{C}}} = \frac{\partial \Psi_{\mathrm{ani}}(\overline{\lambda}_{\mathrm{i}})}{\partial \overline{\lambda_i}^2}\frac{\partial \overline{\lambda_i}^2}{\partial \overline{\mathbf{C}}} = \frac{\partial \Psi_{\mathrm{ani}}(\overline{\lambda}_{\mathrm{i}})}{\partial \overline{\lambda_i}^2}\mathbf{r} \otimes \mathbf{r} \tag{A.11}$$

where $\mathbf{r}$ is the orientation vector in the material configuration and making a variable change $\eta = \overline{\lambda_i}^2$ and taking the last equation into Fig. A.9

$$\overline{\boldsymbol{\tau}}_{\mathrm{ani}} = \overline{\lambda_i}^{-1}\frac{\partial \Psi_{\mathrm{ani}}(\overline{\lambda}_{\mathrm{i}})}{\partial \overline{\lambda}_i}\overline{\mathbf{t}} \otimes \overline{\mathbf{t}} \tag{A.12}$$

Operating in a similar way and taking the first order expansion of $\mathbf{S}$ at $\mathbf{F}$, $\mathrm{d}\mathbf{S} = \mathbf{C} : \mathrm{d}\mathbf{C}/2$ and after some mathematical manipulation (see Holzapfel (2000))

$$\mathbf{C} = \mathbf{C}_{\mathrm{vol}} + \mathbf{C}_{\mathrm{ich}} = 2\left[\frac{\partial \mathbf{S}_{\mathrm{vol}}(\mathrm{J})}{\partial \mathbf{C}} + \frac{\partial \mathbf{S}_{\mathrm{ich}}(\overline{\mathbf{C}})}{\partial \mathbf{C}}\right] \tag{A.13}$$

$$\mathbf{C}_{\mathrm{vol}} = 2\frac{\partial \mathbf{S}_{\mathrm{vol}}(\mathrm{J})}{\partial \mathbf{C}} = J\left[p + J\frac{\mathrm{d}p}{\mathrm{d}J}\right]\mathbf{C}^{-1} \otimes \mathbf{C}^{-1} - 2Jp\mathbf{C}^{-1} \odot \mathbf{C}^{-1} \tag{A.14}$$

$$\mathbf{C}_{\mathrm{iso}} = 2\frac{\partial \mathbf{S}_{\mathrm{iso}}(\overline{\mathbf{C}})}{\partial \mathbf{C}} = \mathbf{P} : \overline{\mathbf{C}} : \mathbf{P}^T + \tfrac{2}{3}Tr\left[J^{-2/3}\overline{\boldsymbol{S}}_{\mathrm{iso}}\right]\widetilde{\mathbf{P}} - \frac{2}{3}\left[\mathbf{C}^{-1} \otimes \mathbf{S}_{\mathrm{iso}} + \mathbf{S}_{\mathrm{iso}} \otimes \mathbf{C}^{-1}\right] \tag{A.15}$$

$$\mathbf{C}_{\mathrm{ani}} = \overline{\lambda_i}^{-2}\left[\frac{\partial^2 \Psi_{\mathrm{ani}}(\overline{\lambda}_{\mathrm{i}})}{\partial \overline{\lambda_i}\partial \overline{\lambda_i}} - \overline{\lambda_i}^{-1}\frac{\partial \Psi_{\mathrm{ani}}(\overline{\lambda}_{\mathrm{i}})}{\partial \overline{\lambda_i}}\right]\overline{\mathbf{t}} \otimes \overline{\mathbf{t}} \otimes \overline{\mathbf{t}} \otimes \overline{\mathbf{t}} \tag{A.16}$$

the associated elasticity tensor in spatial description can be obtained using $\mathbf{C}$ towards $\mathbf{c} = J^{-1}\chi_*(\mathbf{C})$

$$J\mathbf{c}_{\mathrm{vol}} = J(p + J\frac{dp}{dJ})\mathbf{I} \otimes \mathbf{I} - 2pI \tag{A.17}$$

$$J\mathbf{c}_{\mathrm{iso}} = \mathbf{p} : \overline{\mathbf{c}} : \mathbf{p}^T + \frac{2}{3}tr[J^{-2/3}\overline{\boldsymbol{\tau}}]\widetilde{\mathbf{p}} - \frac{2}{3}\left[\mathbf{I} \otimes \boldsymbol{\tau}_{\mathrm{iso}} + \boldsymbol{\tau}_{\mathrm{iso}} \otimes \mathbf{I}\right] \tag{A.18}$$

$$\mathbf{c}_{ani} = \langle \overline{\lambda_i}^{-2} \left[\frac{\partial^2 \Psi_{\rm iso}(\overline{\lambda_{\rm i}})}{\partial \overline{\lambda_i} \partial \overline{\lambda_i}} - \frac{\partial \Psi_{\rm iso}(\overline{\lambda_{\rm i}})}{\overline{\lambda_{\rm i}} \partial \overline{\lambda_i}} \right] \overline{\mathbf{t}} \otimes \overline{\mathbf{t}} \otimes \overline{\mathbf{t}} \otimes \overline{\mathbf{t}} \rangle \tag{A.19}$$

All these tensor must be modified with the introduction of the damage model. Although the stress tensor transforms in a straight way, do not the elastic tensors. In order to obtain them, and making use of the time derivative of $\mathbf{S}$

$$\dot{\mathbf{S}} = \left[[1-D] 2 \frac{\partial \mathbf{S}_0}{\partial \mathbf{C}} \right] : \tfrac{1}{2} \dot{\mathbf{C}} - \mathbf{S}_0 \dot{D} = \left[[1-D] \mathbf{C}_0 - \frac{\mathrm{d}D}{\mathrm{d}\Xi} \mathbf{S}_0 \otimes \mathbf{S}_0 \right] : \frac{1}{2} \dot{\mathbf{C}} \tag{A.20}$$

that related with $d\mathbf{S} = \mathbf{C} : d\mathbf{C}/2$

$$\mathbf{C} = [1-D] \mathbf{C}_0 - \frac{\mathrm{d}D}{\mathrm{d}\Xi} \mathbf{S}_0 \otimes \mathbf{S}_0 \tag{A.21}$$

or in the micro-sphere framework

$$\mathbf{c}_{\rm iso} = [1-D] \mathbf{c}_{0,\rm iso} - \frac{\mathrm{d}D_M}{\mathrm{d}\Xi_M} \boldsymbol{\tau}_{0,\rm iso} \otimes \boldsymbol{\tau}_{0,\rm iso} \tag{A.22}$$

$$\mathbf{c}_{\rm ani} = \langle \overline{\lambda_i}^{-2} [g_f(\Psi''_{\rm iso}(\overline{\lambda_{\rm i}}) - {\lambda_i}^{-1} \Psi'_{\rm iso}(\overline{\lambda_{\rm i}})] + g_f(\Xi_i)' \Psi'^2_{\rm iso}(\overline{\lambda_{\rm i}}) \overline{\mathbf{t}} \otimes \overline{\mathbf{t}} \otimes \overline{\mathbf{t}} \otimes \overline{\mathbf{t}} \rangle \tag{A.23}$$

Bibliography

V. Alastrué, et al. (2009a). 'Anisotropic micro-sphere-based finite elasticity applied to blood vessel modelling'. *J Mech Phys Solids* **57**(1):178–203.

V. Alastrué, et al. (2009b). 'On the use of non-linear transformations for the evaluation of anisotropic rotationally symmetric directional integrals. Application to the stress analysis in fibred soft tissues'. *Intl J Numer Meth Eng* **79**(4):474–504.

V. Alastrué, et al. (2007). 'Structural damage models for fibrous biological soft tissues'. *Int J Solids Struct* **44**(18-19):5894–5911.

E. M. Arruda & M. C. Boyce (1993). 'A three-dimensional constitutive model for the large stretch behavior of rubber elastic materials'. *J Mech Phys Solids* **41**(2):389–412.

G. A. Ateshian (2007). 'On the theory of reactive mixtures for modeling biological growth'. *Biomech Model Mechan* **6**(6):423–445.

P. Bažant & B. H. Oh (1986). 'Efficient Numerical Integration on the Surface of a Sphere'. *ZAMM - Journal of Applied Mathematics and Mechanics / Zeitschrift für Angewandte Mathematik und Mechanik* **66**(1):37–49.

C. Bingham (1974). 'An Antipodally Symmetric Distribution on the Sphere'. *Ann Stat* **2**(6):1201–1225.

J. P. Boehler (1987). *Applications of Tensor Functions in Solid Mechanics*. CISM Courses and Lectures. Springer-Verlag.

B. Calvo, et al. (2007). 'An uncoupled directional damage model for fibred biological soft tissues. Formulation and computational aspects'. *Int J Numer Meth Eng* **69**(10):2036–2057.

T. E. Carew, et al. (1968). 'Compressibility of the Arterial Wall'. *Circ Res* **23**(1):61–68.

C. J. Chuong & Y. C. Fung (1984). 'Compressibility and constitutive equation of arterial wall in radial compression experiments'. *J Biomech* **17**(1):35–40.

H. Demiray, et al. (1988). 'A stress-strain relation for a rat abdominal aorta'. *J Biomech* **21**(5):369–374.

A. E. Ehret & M. Itskov (2009). 'Modeling of anisotropic softening phenomena: Application to soft biological tissues'. *Int J Plasticity* **25**(5):901–919.

P. J. Flory (1961). 'Thermodynamic relations for high elastic materials'. *T Faraday Soc* **57**:829–838.

Y. C. Fung (1990). *Biomechanics: Mechanical Properties of Living Tissues*. Springer.

T. C. Gasser & G. A. Holzapfel (2007). 'Finite element modeling of balloon angioplasty by considering overstretch of remnant non-diseased tissues in lesions'. *Comput Mech* **40**(1):47–60.

T. C. Gasser, et al. (2006). 'Hyperelastic modelling of arterial layers with distributed collagen fibre orientations'. *J Roy Soc Interface* **3**:15–35.

S. Göktepe & C. Miehe (2005). 'A micro-macro approach to rubber-like materials. Part III: The micro-sphere model of anisotropic Mullins-type damage'. *J Mech Phys Solids* **53**(10):2259–2283.

C. S. Herz (1955). 'Bessel Functions of Matrix Argument'. *Ann Math* **61**(3):474–523.

G. Himpel, et al. (2008). 'Time-dependent fibre reorientation of transversely isotropic continua - Finite element formulation and consistent linearization'. *Intl J Numer Meth Eng* **73**(10):1413–1433.

G. A. Holzapfel (2000). *Nonlinear Solid Mechanics: A Continuum Approach for Engineering*. John Wiley & Sons.

G. A. Holzapfel, et al. (2000). 'A New Constitutive Framework for Arterial Wall Mechanics and a Comparative Study of Material Models'. *J Elasticity* **V61**(1):1–48.

G. A. Holzapfel, et al. (2005). 'Determination of layer-specific mechanical properties of human coronary arteries with nonatherosclerotic intimal thickening and related constitutive modeling'. *Am J Physiol Heart Circ Physiol* **289**(5):H2048–2058.

J. D. Humphrey (1995). 'Mechanics of the arterial wall: Review and directions'. *Crit. Rev. Bio. Eng.* **23**(1-2):1–162.

E. Kuhl, et al. (2005). 'Remodeling of biological tissue: Mechanically induced reorientation of a transversely isotropic chain network'. *J Mech Phys Solids* **53**(7):1552–1573.

E. Kuhl & G. Holzapfel (2007). 'A continuum model for remodeling in living structures'. *J Mater Sci* **42**(21):8811–8823.

E. Kuhl, et al. (2006). 'On the convexity of transversely isotropic chain network models'. *Philos Mag* **86**:3241–3258.

M. Landuyt (2006). 'Structural quantification of collagen fibers in Abdominal Aortic Aneurysms'. Master's thesis, Royal Institute of Technology in Stockholm, Department of Solid Mechanics and Ghent University, Department of Civil Engineering.

A. Menzel, et al. (2007). 'Towards an orientation–distribution–based multi–scale approach for remodelling biological tissues'. *Computer Methods in Biomechanics and Biomedical Engineering* . Accepted for publication.

A. Menzel & P. Steinmann (2003). 'A view on anisotropic finite hyper-elasticity'. *Eur J Mech A/Solids* **22**(1):71–87.

A. Menzel & T. Waffenschmidt (2009). 'A microsphere-based remodelling formulation for anisotropic biological tissues'. *Philos. Trans. R. Soc. London, Ser. A* **367**(1902):3499–3523.

C. Miehe (1995). 'Discontinuous and Continuous Damage Evolution In Ogden-type Large-strain Elastic-materials'. *Eur. J. Mech. A. Solids* **14**(5):697–720.

C. Miehe & S. Göktepe (2005). 'A micro-macro approach to rubber-like materials. Part II: The micro-sphere model of finite rubber viscoelasticity'. *J Mech Phys Solids* **53**(10):2231–2258.

C. Miehe, et al. (2004). 'A micro-macro approach to rubber-like materials–Part I: the non-affine micro-sphere model of rubber elasticity'. *J Mech Phys Solids* **52**(11):2617–2660.

A. N. Natali, et al. (2005). 'Anisotropic elasto-damage constitutive model for the biomechanical analysis of tendons'. *Med. Eng. Phys.* **27**(3):209–214.

E. A. D. Neto, et al. (1998). 'Continuum modelling and numerical simulation of material damage at finite strains'. *Arch. Comput. Meth. Eng.* **5**(4):311–384.

R. W. Ogden (1996). *Non-Linear Elastic Deformations*. Dover Publications.

H. Oktay (1994). 'Continuum damage mechanics of ballon angioplasty.'. In *Internal Report*. UMI.

E. Peña, et al. (2010). 'A constitutive formulation of vascular tissue mechanics including viscoelasticity and softening behaviour'. *J Biomech* **43**(5):984–989.

E. Peña & M. Doblaré (2009). 'An anisotropic pseudo-elastic approach for modelling Mullins effect in fibrous biological materials'. *Mech Res Commun* **36**(7):784–790.

J. A. G. Rhodin (1980). *Handbook of Physiology, The Cardiovascular System*, vol. 2, chap. Architecture of the vessel wall, pp. 1–31. American Physiological Society, Bethesda, Maryland.

E. K. Rodriguez, et al. (1994). 'Stress-dependent finite growth in soft elastic tissues'. *J Biomech* **27**(4):455–467.

J. C. Simo (1987). 'On a fully three-dimensional finite-strain viscoelastic damage model: Formulation and computational aspects'. *Comput Method Appl M* **60**(2):153–173.

J. C. Simo & T. J. R. Hughes (1998). *Computational Inelasticity*. Springer.

A. J. M. Spencer (1954). 'Theory of Invariants'. In *Continuum Physiscs*, pp. 239–253. Academic Press, New York.

P. Steinmann (1999). 'Formulation and computation of geometrically non-linear gradient damage'. *Intl J Numer Meth Eng* **46**(5):757–779.

L. A. Taber (1998). 'A model for aortic growth based on fluid shear and fiber stresses'. *J Biomech Eng-T ASME* **120**(3):348–354.

C. Truesdell & W. Noll (2004). *The Non-Linear Field Theories of Mechanics*. Springer-Verlag, 3rd edn.

E. W. Weisstein (2004). '"Erfi." From MathWorld–A Wolfram Web Resource. http://mathworld.wolfram.com/Erfi.html' .